

1

<sup>2</sup>A SEARCH FOR LONG-LIVED, CHARGED, SUPERSYMMETRIC PARTICLES  
<sup>3</sup>USING IONIZATION WITH THE ATLAS DETECTOR

4

BRADLEY AXEN

5

September 2016 – Version 0.26

6



<sup>8</sup> Bradley Axen: *A Search for Long-Lived, Charged, Supersymmetric Particles using Ion-  
<sup>9</sup> ization with the ATLAS Detector*, Subtitle, © September 2016

<sup>10</sup>

Usually a quotation.

<sup>11</sup>

Dedicated to.



<sub>12</sub> ABSTRACT

---

<sub>13</sub> How to write a good abstract:

<sub>14</sub> <https://plg.uwaterloo.ca/~migod/research/beck00PSLA.html>



<sub>15</sub> PUBLICATIONS

---

<sub>16</sub> Some ideas and figures have appeared previously in the following publications:

<sub>17</sub>

<sub>18</sub> Put your publications from the thesis here. The packages `multibib` or `bibtopic`  
<sub>19</sub> etc. can be used to handle multiple different bibliographies in your document.



---

<sup>21</sup> ACKNOWLEDGEMENTS

<sup>22</sup> Put your acknowledgements here.

<sup>23</sup>

<sup>24</sup> And potentially a second round.

<sup>25</sup>



26 CONTENTS

---

27	I	INTRODUCTION	1
28	1	INTRODUCTION	3
29	II	THEORETICAL CONTEXT	5
30	2	STANDARD MODEL	7
31	2.1	Particles . . . . .	7
32	2.2	Interactions . . . . .	8
33	2.3	Limitations . . . . .	8
34	3	SUPERSYMMETRY	9
35	3.1	Motivation . . . . .	9
36	3.2	Structure . . . . .	9
37	3.3	Phenomenology . . . . .	9
38	4	LONG-LIVED PARTICLES	11
39	4.1	Mechanisms . . . . .	11
40	4.1.1	Examples in Supersymmetry . . . . .	11
41	4.2	Phenomenology . . . . .	11
42	4.2.1	Disimilarities to Prompt Decays . . . . .	11
43	4.2.2	Characteristic Signatures . . . . .	11
44	III	EXPERIMENTAL STRUCTURE AND RECONSTRUCTION	13
45	5	THE LARGE HADRON COLLIDER	15
46	5.1	Injection Chain . . . . .	15
47	5.2	Design and Parameters . . . . .	15
48	5.3	Luminosity . . . . .	15
49	6	THE ATLAS DETECTOR	17
50	6.1	Coordinate System . . . . .	17
51	6.2	Magnetic Field . . . . .	17
52	6.3	Inner Detector . . . . .	17
53	6.3.1	Pixel Detector . . . . .	17
54	6.3.2	Semiconductor Tracker . . . . .	17
55	6.3.3	Transition Radiation Tracker . . . . .	17
56	6.4	Calorimetry . . . . .	17
57	6.4.1	Electromagnetic Calorimeters . . . . .	17
58	6.4.2	Hadronic Calorimeters . . . . .	17
59	6.4.3	Forward Calorimeters . . . . .	17
60	6.5	Muon Spectrometer . . . . .	17
61	6.6	Trigger . . . . .	17
62	6.6.1	Trigger Scheme . . . . .	17
63	6.6.2	Missing Transverse Energy Triggers . . . . .	17
64	7	EVENT RECONSTRUCTION	19
65	7.1	Tracks and Vertices . . . . .	19

66	7.1.1	Track Reconstruction . . . . .	19
67	7.1.2	Vertex Reconstruction . . . . .	19
68	7.2	Jets . . . . .	19
69	7.2.1	Topological Clustering . . . . .	19
70	7.2.2	Jet Energy Scale . . . . .	19
71	7.2.3	Jet Energy Scale Uncertainties . . . . .	19
72	7.2.4	Jet Energy Resolution . . . . .	19
73	7.3	Electrons . . . . .	19
74	7.3.1	Electron Identification . . . . .	19
75	7.4	Muons . . . . .	19
76	7.4.1	Muon Identification . . . . .	19
77	7.5	Missing Transverse Energy . . . . .	19
78	IV	CALORIMETER RESPONSE	21
79	8	RESPONSE MEASUREMENT WITH SINGLE HADRONS	23
80	8.1	Dataset and Simulation . . . . .	24
81	8.1.1	Data Samples . . . . .	24
82	8.1.2	Simulated Samples . . . . .	24
83	8.1.3	Event Selection . . . . .	24
84	8.2	Inclusive Hadron Response . . . . .	25
85	8.2.1	E/p Distribution . . . . .	26
86	8.2.2	Zero Fraction . . . . .	26
87	8.2.3	Neutral Background Subtraction . . . . .	28
88	8.2.4	Corrected Response . . . . .	28
89	8.3	Identified Particle Response . . . . .	34
90	8.3.1	Decay Reconstruction . . . . .	34
91	8.3.2	Identified Response . . . . .	35
92	8.3.3	Additional Species in Simulation . . . . .	37
93	8.4	Summary . . . . .	38
94	9	JET ENERGY RESPONSE AND UNCERTAINTY	41
95	9.1	Motivation . . . . .	41
96	9.2	Uncertainty Estimate . . . . .	41
97	9.3	Summary . . . . .	44
98	V	SEARCH FOR LONG-LIVED PARTICLES	47
99	10	LONG-LIVED PARTICLES IN ATLAS	49
100	10.1	Overview and Characteristics . . . . .	49
101	10.2	Simulation . . . . .	49
102	11	EVENT SELECTION	51
103	11.1	Trigger . . . . .	52
104	11.2	Kinematics and Isolation . . . . .	52
105	11.3	Standard Model Rejection . . . . .	55
106	11.4	Ionization . . . . .	58
107	11.4.1	dE/dx Calibration . . . . .	58
108	11.4.2	Mass Estimation . . . . .	58
109	12	BACKGROUND ESTIMATION	61

110	12.1	Background Sources . . . . .	61
111	12.2	Prediction Method . . . . .	61
112	12.3	Validation and Uncertainty . . . . .	61
113	13	SYSTEMATIC UNCERTAINTIES AND RESULTS	63
114	13.1	Systematic Uncertainties . . . . .	63
115	13.2	Final Yields . . . . .	63
116	14	INTERPRETATION	65
117	14.1	Cross Sectional Limits . . . . .	65
118	14.2	Mass Limits . . . . .	65
119	14.3	Context for Long-Lived Searches . . . . .	65
120	VI	CONCLUSIONS	67
121	15	SUMMARY AND OUTLOOK	69
122	15.1	Summary . . . . .	69
123	15.2	Outlook . . . . .	69
124	VII	APPENDIX	71
125	A	INELASTIC CROSS SECTION	73
126	B	APPENDIX TEST	75
127	B.1	Appendix Section Test . . . . .	75
128	B.1.1	Appendix Subection Test . . . . .	75
129	B.2	A Table and Listing . . . . .	75
130	B.3	Some Formulas . . . . .	76
131		BIBLIOGRAPHY	79

132 LIST OF FIGURES

---

133	Figure 1	The particle content of the Standard Model (SM). . . . .	8
134	Figure 2	An illustration (a) of the $E/p$ variable used throughout this paper. The red energy deposits come from the charged particle targeted for measurement, while the blue energy deposits are from nearby neutral particles and must be subtracted. The same diagram (b) for the neutral-background selection, described in Section 8.2.3.	25
135			
136			
137			
138			
139			
140	Figure 3	The $E/p$ distribution and ratio of simulation to data for isolated tracks with (a) $ \eta  < 0.6$ and $1.2 < p/\text{GeV} < 1.8$ and (b) $ \eta  < 0.6$ and $2.2 < p/\text{GeV} < 2.8$ . . . . .	26
141			
142			
143	Figure 4	The fraction of tracks as a function (a, b) of momentum, (c, d) of interaction lengths with $E \leq 0$ for tracks with positive (on the left) and negative (on the right) charge. . . . .	27
144			
145			
146			
147	Figure 5	$\langle E/p \rangle_{\text{BG}}$ as a function of the track momentum for tracks with (a) $ \eta  < 0.6$ , (b) $0.6 <  \eta  < 1.1$ , and as a function of the track pseudorapidity for tracks with (c) $1.2 < p/\text{GeV} < 1.8$ , (d) $1.8 < p/\text{GeV} < 2.2$ . . . . .	29
148			
149			
150			
151	Figure 6	$\langle E/p \rangle_{\text{COR}}$ as a function of track momentum, for tracks with (a) $ \eta  < 0.6$ , (b) $0.6 <  \eta  < 1.1$ , (c) $1.8 <  \eta  < 1.9$ , and (d) $1.9 <  \eta  < 2.3$ . . . . .	30
152			
153			
154	Figure 7	$\langle E/p \rangle_{\text{COR}}$ calculated using LCW-calibrated topological clusters as a function of track momentum for tracks with (a) zero or more associated topological clusters or (b) one or more associated topological clusters. . . . .	31
155			
156			
157			
158	Figure 8	Comparison of the $\langle E/p \rangle_{\text{COR}}$ for tracks with (a) less than and (b) greater than 20 hits in the TRT. . . . .	32
159			
160	Figure 9	Comparison of the $\langle E/p \rangle_{\text{COR}}$ for (a) positive and (b) negative tracks as a function of track momentum for tracks with $ \eta  < 0.6$ . . . . .	32
161			
162			
163	Figure 10	Comparison of the $E/p$ distributions for (a) positive and (b) negative tracks with $0.8 < p/\text{GeV} < 1.2$ and $ \eta  < 0.6$ , in simulation with the FTFP_BERT and QGSP_BERT physics lists. . . . .	33
164			
165			
166			
167	Figure 11	Comparison of the response of the hadronic calorimeter as a function of track momentum (a) at the EM-scale and (b) after the LCW calibration. . . . .	33
168			
169			
170	Figure 12	Comparison of the response of the EM calorimeter as a function of track momentum (a) at the EM-scale and (b) with the LCW calibration. . . . .	34
171			
172			

173	Figure 13	The reconstructed mass peaks of (a) $K_S^0$ , (b) $\Lambda$ , and (c) $\bar{\Lambda}$ candidates. . . . .	35
174			
175	Figure 14	The $E/p$ distribution for isolated (a) $\pi^+$ , (b) $\pi^-$ , (c) proton, and (d) anti-proton tracks. . . . .	36
176			
177	Figure 15	The fraction of tracks with $E \leq 0$ for identified (a) $\pi^+$ and $\pi^-$ , and (b) proton and anti-proton tracks . . . . .	36
178			
179	Figure 16	The difference in $\langle E/p \rangle$ between (a) $\pi^+$ and $\pi^-$ (b) $p$ and $\pi^+$ , and (c) $\bar{p}$ and $\pi^-$ . . . . .	37
180			
181	Figure 17	$\langle E/p \rangle_{\text{COR}}$ as a function of track momentum for (a) $\pi^+$ tracks and (b) $\pi^-$ tracks. . . . .	38
182			
183	Figure 18	The ratio of the calorimeter response to single parti- cles of various species to the calorimeter response to $\pi^+$ with the physics list FTFP_BERT. . . . .	38
184			
185	Figure 19	The spectra of true particles inside anti- $k_t$ , $R = 0.4$ jets with (a) $90 < p_T/\text{GeV} < 100$ , (b) $400 < p_T/\text{GeV} <$ $500$ , and (c) $1800 < p_T/\text{GeV} < 2300$ . . . . .	42
186			
187	Figure 20	The jet energy scale ( $\text{JES}$ ) uncertainty contributions, as well as the total $\text{JES}$ uncertainty, as a function of jet $p_T$ for (a) $ \eta  < 0.6$ and (b) $0.6 <  \eta  < 1.1$ . . . . .	44
188			
189	Figure 21	The $\text{JES}$ correlations as a function of jet $p_T$ and $ \eta $ for jets in the central region of the detector. . . . .	45
190			
191	Figure 22	The trigger efficiency of the $E_T^{\text{miss}}$ trigger as a function of mass and lifetime. . . . .	52
192			
193	Figure 23	The distribution of $E_T^{\text{miss}}$ for data and simulated signal events, after the trigger requirement. . . . .	53
194			
195	Figure 24	The dependence of $dE/dx$ on $N_{\text{split}}$ in data after basic track hit requirements have been applied. . . . .	54
196			
197	Figure 25	The distribution of $dE/dx$ with various selections ap- plied in data and simulated signal events. . . . .	55
198			
199	Figure 26	The distribution of track momentum for data and sim- ulated signal events, after previous selection require- ments have been applied. . . . .	56
200			
201	Figure 27	The distribution of $M_T$ for data and simulated sig- nal events, after previous selection requirements have been applied. . . . .	57
202			
203	Figure 28	The distribution of summed tracked momentum within a cone of $\Delta R < 0.25$ around the candidate track for data and simulated signal events, after previous selec- tion requirements have been applied. . . . .	58
204			
205	Figure 29	The normalized, two-dimensional distribution of $E/p$ and $f_{\text{EM}}$ for simulated (a) $Z \rightarrow ee$ , (b) $Z \rightarrow \tau\tau$ , (c) 1200 GeV Stable R-Hadron events, and (d) 1200 GeV, 10 ns R-Hadron events. . . . .	59
206			
207			
208			
209			
210			
211			
212			
213			
214			
215			

<sub>216</sub> LIST OF TABLES

---

<sub>217</sub>	Table 1	The dominant sources of corrections and systematic uncertainties in the JES estimation technique, includ- ing typical values for the correcting shift ( $\Delta$ ) and the associated uncertainty ( $\sigma$ ). . . . . .	<sub>43</sub>
<sub>218</sub>			
<sub>219</sub>			
<sub>220</sub>	Table 2	Autem usu id . . . . .	<sub>75</sub>
<sub>221</sub>			

222 LISTINGS

---

<small>223</small> Listing 1	A floating example ( <code>listings</code> manual)	76
------------------------------	--	----

<sup>224</sup> ACRONYMS

---

- <sup>225</sup> SM Standard Model
- <sup>226</sup> LSP Lightest Supersymmetric Particle
- <sup>227</sup> LHC Large Hadron Collider
- <sup>228</sup> ToT time over threshold
- <sup>229</sup> LCW local cluster weighted
- <sup>230</sup> MIP minimally ionizing particle
- <sup>231</sup> EPJC European Physical Journal C
- <sup>232</sup> JES jet energy scale
- <sup>233</sup> LLP Long-Lived Particle

234

## PART I

235

### INTRODUCTION

236

You can put some informational part preamble text here.



# 1

237

238 INTRODUCTION

---



239

## PART II

240

### THEORETICAL CONTEXT

241

You can put some informational part preamble text here.



# 2

242

## 243 STANDARD MODEL

---

244 The SM of particle physics seeks to explain the symmetries and interactions of  
245 all currently discovered fundamental particles. It has been tested by several genera-  
246 tions of experiments and has been remarkably successful, no significant de-  
247 viations have been found. The SM provides predictions in particle physics for  
248 interactions up to the Planck scale ( $10^{15}$ - $10^{19}$  GeV).

249 The theory itself is a quantum field theory grown from an underlying  $SU(3) \times$   
250  $SU(2) \times U(1)$  that requires the particle content and quantum numbers consist-  
251 ent with experimental observations (see Section 2.1). Each postulated symme-  
252 try is accompanied by an interaction between particles through gauge invari-  
253 ance. These interactions are referred to as the Strong, Weak, and Electromag-  
254 netic forces, which are discussed in Section 2.2.

255 Although this model has been very predictive, the theory is incomplete; for  
256 example, it is not able to describe gravity or astronomically observed dark matter.  
257 These limitations are discussed in more detail in Section 2.3.

## 258 21 PARTICLES

259 The most familiar matter in the universe is made up of protons, neutrons, and  
260 electrons. Protons and neutrons are composite particles, however, and are made  
261 up in turn by particles called quarks. Quarks carry both electric charge and color  
262 charge, and are bound in color-neutral combinations called baryons. The elec-  
263 tron is an example of a lepton, and carries only electric charge. Another type  
264 of particle, the neutrino, does not form atomic structures in the same way that  
265 quarks and leptons do because it carries no color or electric charge. Collectively,  
266 these types of particles are known as fermions, the group of particles with half-  
267 integer spin.

268 There are three generations of fermions, although familiar matter is formed  
269 predominantly by the first generation. The generations are identical except for  
270 their masses, which increase in each generation by convention. In addition, each  
271 of these particles is accompanied by an antiparticle, with opposite-sign quantum  
272 numbers but the same mass.

273 The fermions comprise what is typically considered matter, but there are  
274 additional particles that are mediators of interactions between those fermions.  
275 These mediators are known as the gauge bosons, gauge in that their existence  
276 is required by gauge invariance (discussed further in Section 2.2) and bosons in  
277 that they have integer spin. The boson which mediates the electromagnetic force  
278 is the photon, the first boson to be discovered; it has no electric charge, no mass,  
279 and a spin of 1. There are three spin-1 mediators of the weak force, the two W  
280 bosons and the Z boson. The W bosons have electric charge of  $\pm 1$  and a mass of  
281  $80.385 \pm 0.015$  GeV, while the Z boson is neutral and has a mass of  $91.1876 \pm$

282 0.0021 GeV. The strong force is mediated by eight particles called gluons, which  
 283 are massless and electrically neutral but do carry color charge.

284 The final particle present in the SM is the Higgs boson, which was recently  
 285 observed for the first time by experiments at CERN in 2012. It is electrically  
 286 neutral, has a mass of  $125.7 \pm 0.4$  GeV, and is the only spin-0 particle yet to be  
 287 observed. The Higgs boson is the gauge boson associated with the mechanism  
 288 that gives a mass to the W and Z bosons.

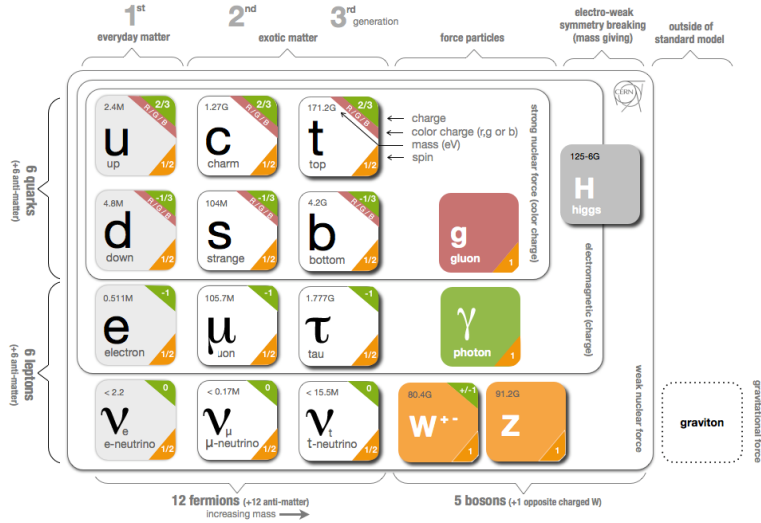


Figure 1: The particle content of the SM.

289 Together these particles form the entire content of the SM, and are summa-  
 290 rized in Figure 1. These are the particles that constitute the observable universe  
 291 and all the so-far-observed interactions within it.

## 292 2.2 INTERACTIONS

293 The interactions predicted and described by the SM are fundamentally tied to the  
 294 particles within it, both in that they describe the way those particles can influence  
 295 each other and also in that the existence of the interactions requires the existence  
 296 of some particles (the gauge bosons).

## 297 2.3 LIMITATIONS

# 3

298

299 SUPERSYMMETRY

---

300 3.1 MOTIVATION

301 3.2 STRUCTURE

302 3.3 PHENOMENOLOGY



# 4

303

304 LONG-LIVED PARTICLES

---

305 4.1 MECHANISMS

306 4.1.1 EXAMPLES IN SUPERSYMMETRY

307 4.2 PHENOMENOLOGY

308 4.2.1 DISIMILARITIES TO PROMPT DECAYS

309 4.2.2 CHARACTERISTIC SIGNATURES



310

### PART III

311

## EXPERIMENTAL STRUCTURE AND RECONSTRUCTION

312

You can put some informational part preamble text here.



# 5

313

314 THE LARGE HADRON COLLIDER

---

315 5.1 INJECTION CHAIN

316 5.2 DESIGN AND PARAMETERS

317 5.3 LUMINOSITY



# 6

318

## 319 THE ATLAS DETECTOR

---

320 6.1 COORDINATE SYSTEM

321 6.2 MAGNETIC FIELD

322 6.3 INNER DETECTOR

323 6.3.1 PIXEL DETECTOR

324 6.3.2 SEMICONDUCTOR TRACKER

325 6.3.3 TRANSITION RADIATION TRACKER

326 6.4 CALORIMETRY

327 6.4.1 ELECTROMAGNETIC CALORIMETERS

328 6.4.2 HADRONIC CALORIMETERS

329 6.4.3 FORWARD CALORIMETERS

330 6.5 MUON SPECTROMETER

331 6.6 TRIGGER

332 6.6.1 TRIGGER SCHEME

333 6.6.2 MISSING TRANSVERSE ENERGY TRIGGERS



# 7

334

## 335 EVENT RECONSTRUCTION

---

336 The ATLAS experiment combines measurements in the subdetectors to form a  
337 cohesive picture of each physics event.

### 338 7.1 TRACKS AND VERTICES

#### 339 7.1.1 TRACK RECONSTRUCTION

##### 340 7.1.1.1 NEURAL NETWORK

##### 341 7.1.1.2 PIXEL DE/DX

#### 342 7.1.2 VERTEX RECONSTRUCTION

### 343 7.2 JETS

#### 344 7.2.1 TOPOLOGICAL CLUSTERING

#### 345 7.2.2 JET ENERGY SCALE

#### 346 7.2.3 JET ENERGY SCALE UNCERTAINTIES

#### 347 7.2.4 JET ENERGY RESOLUTION

### 348 7.3 ELECTRONS

#### 349 7.3.1 ELECTRON IDENTIFICATION

### 350 7.4 MUONS

#### 351 7.4.1 MUON IDENTIFICATION

### 352 7.5 MISSING TRANSVERSE ENERGY



353

## PART IV

354

### CALORIMETER RESPONSE

355

You can put some informational part preamble text here.



358 As discussed in Section 7.2, colored particles produced in collisions hadronize  
359 into jets of multiple hadrons. One approach to understanding jet physics in the  
360 ATLAS calorimetry is to evaluate the calorimeter response to those individual  
361 hadrons; measurements of individual hadrons can be used to build up an under-  
362 standing of the jets that they form. The redundancy of the momentum provided  
363 by the tracking system and the energy provided by the calorimeter provides an  
364 opportunity to study calorimeter response using real collisions, as described fur-  
365 ther in Section 8.2.

366 Calorimeter response includes a number of physical effects that can be ex-  
367 tracted to provide insight into many aspects of jet modeling. First, many charged  
368 hadrons interact with the material of the detector prior to reaching the calorime-  
369 ters and thus do not deposit any energy. Comparing this effect in data and sim-  
370 ulation is a powerful tool in validating the interactions of particles with the ma-  
371 terial of the detector and the model of the detector geometry in simulation, see  
372 Section 8.2.2. The particles which do reach the calorimeter deposit their energy  
373 into individual cells, which are then clustered to measure full energy deposits.  
374 Comparing the response in data to simulated hadrons provides a direct evalua-  
375 tion of noise in the calorimeters, the showering of hadronic particles, and the  
376 energy deposited by particles in matter (Section 8.2.4). These measurements are  
377 extended to explore several additional effects, such as the dependence on charge,  
378 in Section 8.2.4.1.

379 The above studies all use an inclusive selection of charged particles, which are  
380 comprised predominantly of pions, kaons, and (anti)protons. It is also possible  
381 to measure the particle types separately to evaluate the simulated interactions of  
382 each particle, particularly at low energies where differences between species are  
383 very relevant. Pions and (anti)protons can be identified through decays of long-  
384 lived particles, in particular  $\Lambda$ ,  $\bar{\Lambda}$ , and  $K_S^0$ , and then used to measure response as  
385 described above. This is discussed in detail in Section 8.3.

386 Together, these measurements in data provide a thorough understanding of  
387 the way hadrons interact with the ATLAS detector and can be used to build up a  
388 description of jets, as seen in Chapter 9. The results in this chapter use data col-  
389 lected at 7 and 8 TeV collected in 2010 and 2012, respectively. Both are included  
390 as the calorimeter was repaired and recalibrated between those two data-taking  
391 periods. Both sets of data are compared to an updated simulation that includes  
392 new physics models provided by Geant4 [12] and improvements in the detec-  
393 tor description [2, 6]. These results are published in European Physical Journal  
394 C (EPJC) [8] and can be compared to a similar measurement performed in 2009  
395 and 2010 [5], which used the previous version of the simulation framework [1].

## 396 8.1 DATASET AND SIMULATION

## 397 8.1.1 DATA SAMPLES

398 The two datasets used in this chapter are taken from dedicated low-pileup runs  
 399 where the fraction of events with multiple interactions was negligible, to facilitate  
 400 measurement of isolated hadrons. The 2012 dataset at  $\sqrt{s} = 8$  TeV contains  
 401 8 million events and corresponds to an integrated luminosity of  $0.1 \text{ nb}^{-1}$ . The  
 402 2010 dataset at  $\sqrt{s} = 7$  TeV contains 3 million events and corresponds to an  
 403 integrated luminosity of  $3.2 \text{ nb}^{-1}$ . The latter dataset was also used in the 2010  
 404 results [5], but it has since been reanalyzed with an updated detector description  
 405 for the material and alignment.

## 406 8.1.2 SIMULATED SAMPLES

407 The two datasets above are compared to simulated single-, double-, and non-  
 408 diffractive events generated with Pythia8 [32] using the A2 configuration of  
 409 hadronization [3] and the MSTW 2008 parton-distribution function set [28, 31].  
 410 The conditions and energies for each run are matched in the two simulations.

411 To evaluate the interaction of hadrons with detector material, the simulation  
 412 uses two different collections of hadronic physics models, called physics lists, in  
 413 Geant4 9.4 [30]. The first, QGSP\_BERT, combines the Bertini intra-nuclear  
 414 cascade [17, 24, 26] below 9.9 GeV, a parametrized proton inelastic model from  
 415 9.5 to 25 GeV [21], and a quark-gluon string model above 12 GeV [13, 14, 18, 19,  
 416 22]. The second, FTFP\_BERT, combines the Bertini intra-nuclear cascade [17, 24,  
 417 26] below 5 GeV and the Fritiof model [15, 16, 23, 29] above 4 GeV. In either list,  
 418 Geant4 enforces a smooth transition between models where multiple models  
 419 overlap.

## 420 8.1.3 EVENT SELECTION

421 The event selection for this study is minimal, as the only requirement is selecting  
 422 good-quality events with an isolated track. Such events are triggered by requiring  
 423 at least two hits in the minimum-bias trigger scintillators. After trigger, each  
 424 event is required to have exactly one reconstructed vertex, and that vertex is re-  
 425 quired to have four or more associated tracks.

426 The particles which enter into the response measurements are first identified  
 427 as tracks in the inner detector. The tracks are required to have at least 500 MeV  
 428 of transverse momentum. To ensure a reliable momentum measurement, these  
 429 tracks are required to have at least one hit in the pixel detector, six hits in the SCT,  
 430 and small longitudinal and transverse impact parameters with respect to the pri-  
 431 mary vertex [5]. For the majority of the measurements in this chapter, the track is  
 432 additionally required to have 20 hits in the TRT, which significantly reduces the  
 433 contribution from tracks which undergo nuclear interactions. This requirement  
 434 and its effect is discussed in more detail in Section 8.2.4.1. In addition, tracks are  
 435 rejected if there is another track which extrapolates to the calorimeter within a

cone of  $\Delta R = \sqrt{(\Delta\phi)^2 + (\Delta\eta)^2} < 0.4$ . This requirement guarantees that the contamination of energy from nearby charged particles is negligible [5].

## 8.2 INCLUSIVE HADRON RESPONSE

The calorimeter response is more precisely defined as the ratio of the measured calorimeter energy to the true energy carried by the particle, although this true energy is unknown. For charged particles, however, the inner detector provides a very precise measurement of momentum (with uncertainty less than 1%) that can be used as a proxy for true energy. The ratio of the energy deposited by the charged particle in the calorimeter,  $E$ , to its momentum measured in the inner detector  $p$ , forms the calorimeter response measure called  $E/p$ . Though the distribution of  $E/p$  contains a number of physical features, this study focuses on the trends in two aggregated quantities:  $\langle E/p \rangle$ , the average of  $E/p$  within a given subset of particles, and the zero fraction, the fraction of particles with no associated energy in the calorimeter.

The calorimeter energy assigned to a track particle is defined using clusters. The clusters are formed using a 4–2–0 algorithm [9] that begins with seeds requiring at least 4 times the average calorimeter noise. The neighboring cells with at least twice that noise threshold are then added to the cluster, and all bounding cells are then added with no requirement. This algorithm minimizes noise contributions through its seeding process, and including the additional layers improves the energy resolution [33]. The clusters are associated to a given track if they fall within a cone of  $\Delta R = 0.2$  of the extrapolated position of the track, which includes about 90% of the energy on average [5]. This construction is illustrated in Figure 2.

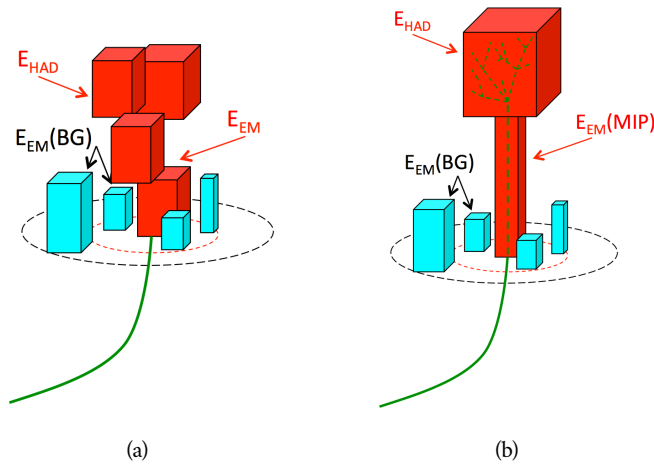
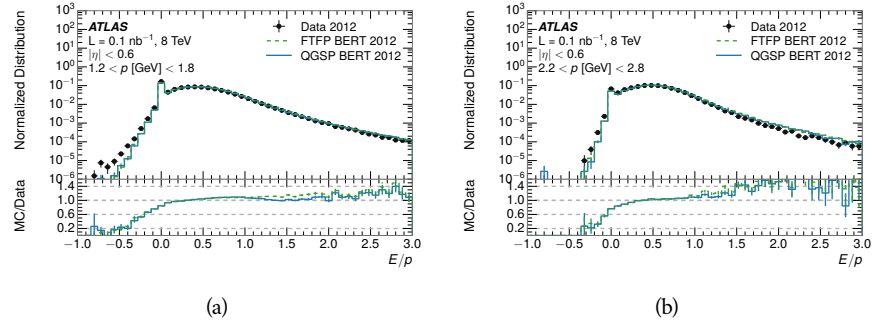


Figure 2: An illustration (a) of the  $E/p$  variable used throughout this paper. The red energy deposits come from the charged particle targeted for measurement, while the blue energy deposits are from nearby neutral particles and must be subtracted. The same diagram (b) for the neutral-background selection, described in Section 8.2.3.

## 460 8.2.1 E/P DISTRIBUTION

461 The  $E/p$  distributions measured in both data and simulation are shown in Figure 3 for two example bins of track momentum and for tracks in the central  
 462 region of the detector. These distributions show several important features of  
 463 the  $E/p$  observable. The large content in the bin at  $E = 0$  comes from tracks that  
 464 have no associated cluster, which occurs due to interactions with detector mate-  
 465 rial prior to reaching the calorimeter or the energy deposit being insufficiently  
 466 large to generate a seed, and are discussed in Section 8.2.2. The small negative  
 467 tail comes from similar tracks that do not deposit any energy in the calorime-  
 468 ter but are randomly associated to a noise cluster. The long positive tail above  
 469 1.0 comes from the contribution of neutral particles. Nearby neutral particles  
 470 deposit (sometimes large) additional energy in the calorimeter but do not pro-  
 471 duce tracks in the inner detector, so they cannot be rejected by the track isol-  
 472 ation requirement. Additionally the peak and mean of the distribution falls below  
 473 1.0 because of the loss of energy not found within the cone as well as the non-  
 474 compensation of the calorimeter.  
 475

476 The data and simulation share the same features, but the high and low tails  
 477 are significantly different. The simulated events tend to overestimate the contri-  
 478 bution of neutral particles to the long tail, an effect which can be isolated and  
 479 removed as discussed in Section 8.2.3. Additionally, the simulated clusters have  
 480 less noise on average, although this is a small effect on the overall response.



481 Figure 3: The  $E/p$  distribution and ratio of simulation to data for isolated tracks with  
 482 (a)  $|\eta| < 0.6$  and  $1.2 < p/\text{GeV} < 1.8$  and (b)  $|\eta| < 0.6$  and  $2.2 < p/\text{GeV} < 2.8$ .

## 483 8.2.2 ZERO FRACTION

484 The fraction of particles with no associated clusters, or similarly those with  $E \leq$   
 485 0, reflects the modeling of both the detector geometry and hadronic interactions.  
 486 The zero fraction is expected to rise as the amount of material a particle traverses  
 487 increases, while it is expected to decrease as the particle energy increases. This  
 488 dependence can be seen in Figure 4, where the zero fraction in data and simula-  
 489 tion is shown as a function of momentum and the amount of material measured  
 in interaction lengths. The trends are similar between the 2010 and 2012 mea-  
 surements. The zero fraction decreases with energy as expected. The amount of

material in the detector increases with  $\eta$ , which provides a distribution of interaction lengths. As the data and simulation have significant disagreement in the zero fraction over a number of interaction lengths, the difference must be primarily from the modeling of hadronic interactions with detector material and not just the detector geometry.

There is also a noticeable difference between positive and negative tracks at low momentum, which reflects the difference in response between protons and antiprotons. Antiprotons have significant model differences in the two physics lists, QGSP\_BERT and FTFP\_BERT, and this is evident in the lowest momentum bin of the data to simulation ratio. This difference is explored further in Section 8.3.

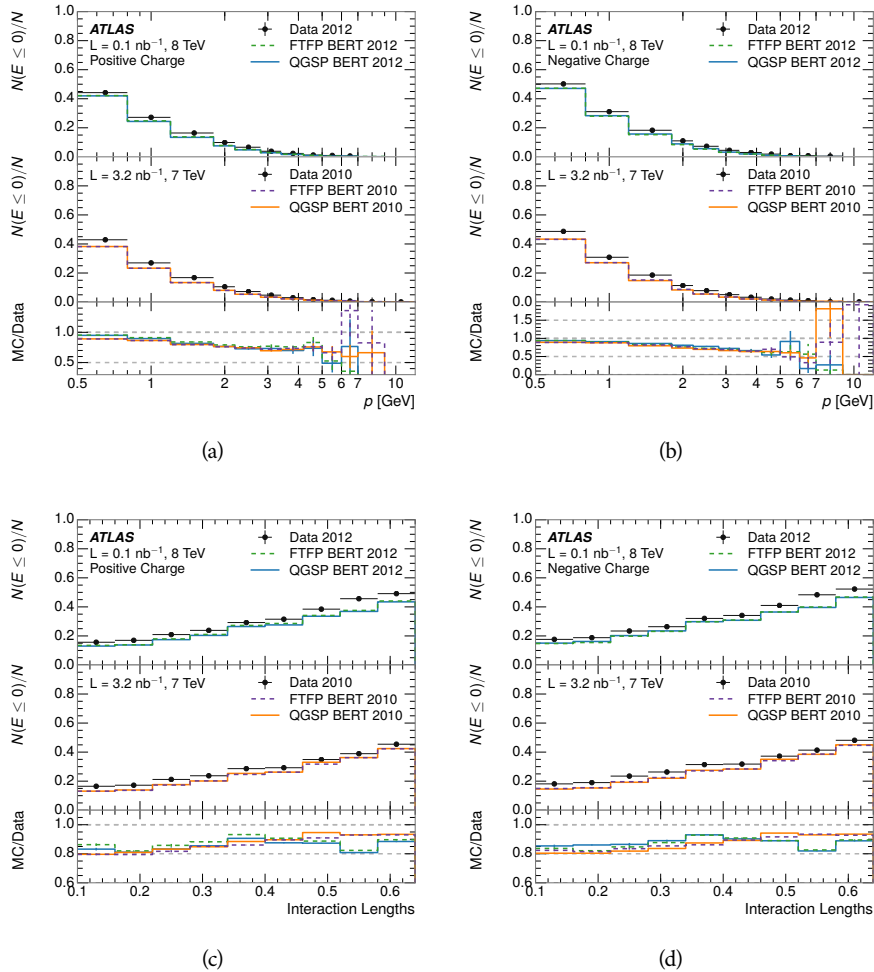


Figure 4: The fraction of tracks as a function (a, b) of momentum, (c, d) of interaction lengths with  $E \leq 0$  for tracks with positive (on the left) and negative (on the right) charge.

## 501 8.2.3 NEUTRAL BACKGROUND SUBTRACTION

502 The isolation requirement on hadrons is only effective in remove energy contri-  
 503 bution from nearby charged particles. Nearby neutral particles, predominantly  
 504 photons from  $\pi^0$  decays, also add their energy to the calorimeter clusters, but  
 505 mostly in the electromagnetic calorimeter. It is possible to measure this contri-  
 506 bution, on average, using late-showering hadrons that minimally ionize in the  
 507 electromagnetic calorimeter. Such particles are selected by requiring that they  
 508 deposit less than 1.1 GeV in the EM calorimeter within a cone of  $\Delta R < 0.1$   
 509 around the track. To ensure that these particles are well measured, they are addi-  
 510 tionally required to deposit between 40% and 90% of their energy in the hadronic  
 511 calorimeter within the same cone.

512 These particles provide a clean sample to measure the nearby neutral back-  
 513 ground because they do not deposit energy in the area immediately surrounding  
 514 them in the EM calorimeter, as shown in Figure 2. So, the energy deposits in the  
 515 region  $0.1 < \Delta R < 0.2$  can be attributed to neutral particles alone. To estimate  
 516 the contribution to the whole cone considered for the response measurement,  
 517 that energy is scaled by a geometric factor of 4/3. This quantity,  $\langle E/p \rangle_{\text{BG}}$ , mea-  
 518 sured in aggregate over a number of particles, gives the contribution to  $\langle E/p \rangle$   
 519 from neutral particles in the EM calorimeter. Similar techniques were used in  
 520 the individual layers of the hadronic calorimeters to show that the background  
 521 from neutrals is negligible in those layers [5].

522 The distribution of this background estimate is shown in Figure 5. Although  
 523 the simulation captures the overall trend, it significantly overestimates the neu-  
 524 tral contribution for tracks with momentum between 2 and 8 GeV. This effect  
 525 was also seen in the tails of the  $E/p$  distributions in Figure 3. This difference is  
 526 likely due to the modeling of coherent neutral particle radiation in Pythia8, as  
 527 the discrepancy does not depend on  $\eta$  and thus is unlikely to be a mismodeling  
 528 of the detector. This difference can be subtracted to form a corrected average  
 529  $E/p$ , as in Section 8.2.4.

## 530 8.2.4 CORRECTED RESPONSE

531 Figure 6 shows  $\langle E/p \rangle_{\text{COR}}$  as a function of momentum for several bins of pseu-  
 532 dorapidity. This corrected  $\langle E/p \rangle_{\text{COR}} \equiv \langle E/p \rangle - \langle E/p \rangle_{\text{BG}}$  measures the average  
 533 calorimeter response without the contamination of neutral particles. It is the  
 534 most direct measurement of calorimeter response in that it is the energy mea-  
 535 sured for fully isolated hadrons. The correction is performed separately in data  
 536 and simulation, so that the mismodeling of the neutral background in simulation  
 537 is removed from the comparison of response. The simulation overestimates the  
 538 response at low momentum by about 5%, an effect that can be mostly attributed  
 539 to the underestimation of the zero fraction mentioned previously.

540 The response measurement above used topological clustering at the EM scale,  
 541 that is clusters were formed to measure energy but no corrections were applied  
 542 to correct for expected effects like energy lost outside of the cluster or in unin-  
 543 strumented material. It is also interesting to measure  $\langle E/p \rangle_{\text{COR}}$  using local clus-

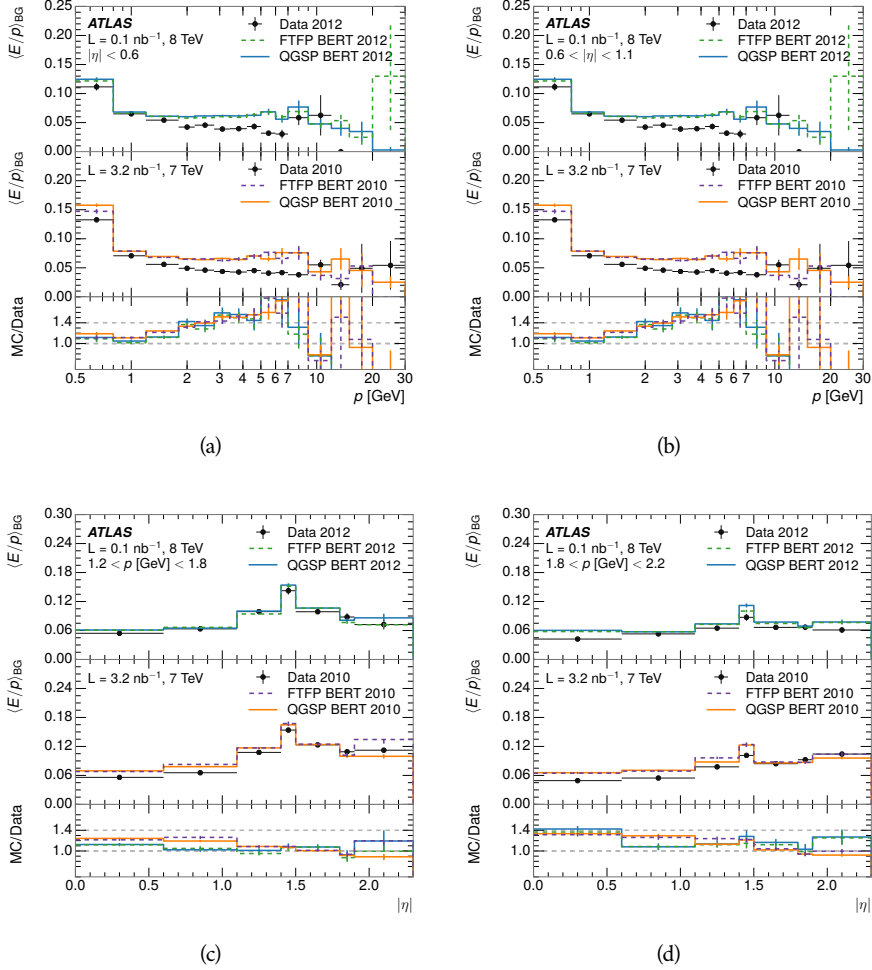


Figure 5:  $\langle E/p \rangle_{\text{BG}}$  as a function of the track momentum for tracks with (a)  $|\eta| < 0.6$ , (b)  $0.6 < |\eta| < 1.1$ , and as a function of the track pseudorapidity for tracks with (c)  $1.2 < p/\text{GeV} < 1.8$ , (d)  $1.8 < p/\text{GeV} < 2.2$ .

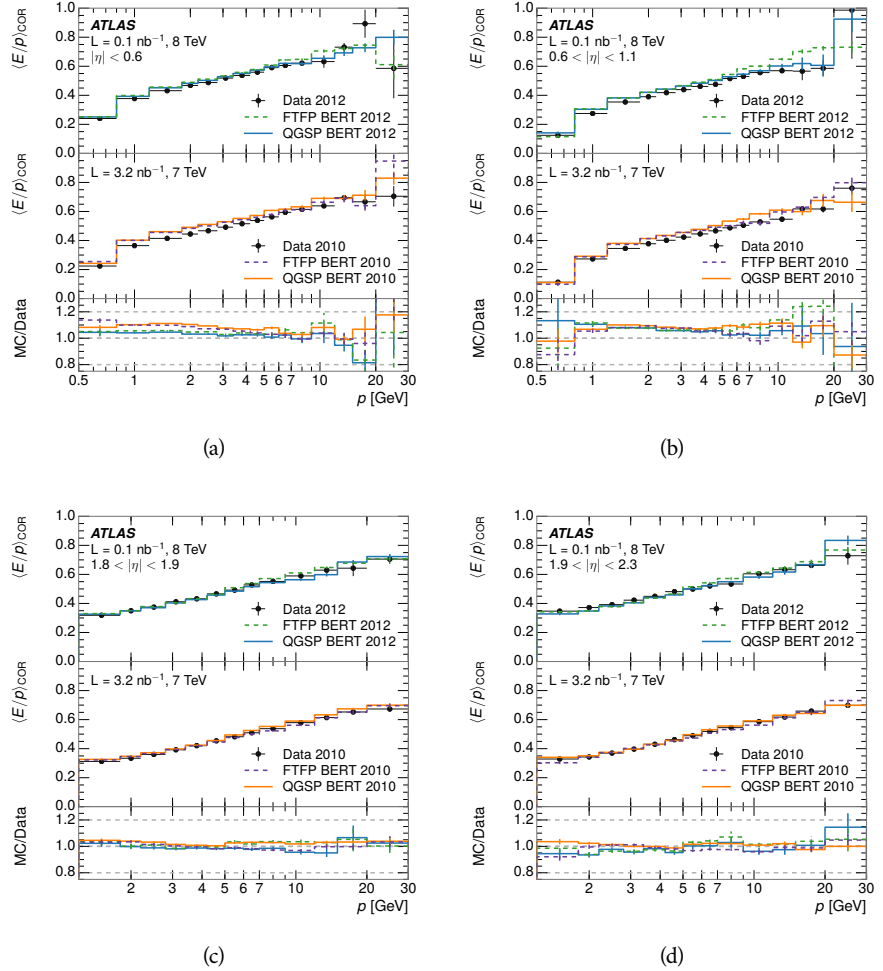


Figure 6:  $\langle E/p \rangle_{\text{COR}}$  as a function of track momentum, for tracks with (a)  $|\eta| < 0.6$ , (b)  $0.6 < |\eta| < 1.1$ , (c)  $1.8 < |\eta| < 1.9$ , and (d)  $1.9 < |\eta| < 2.3$ .

544 ter weighted (LCW) energies, which accounts for those effects by calibrating the  
 545 energy based on the properties of the cluster such as energy density and depth  
 546 in the calorimeter. Figure 7 shows these distributions for tracks with zero or  
 547 more clusters and separately for tracks with one or more clusters. The calibra-  
 548 tion moves  $\langle E/p \rangle_{\text{COR}}$  significantly closer to 1.0, which is the purpose of the cali-  
 549 bration. The agreement between data and simulation improves noticeably when  
 550 at least one cluster is required, as this removes the contribution from the mis-  
 551 modeling of the zero fraction.

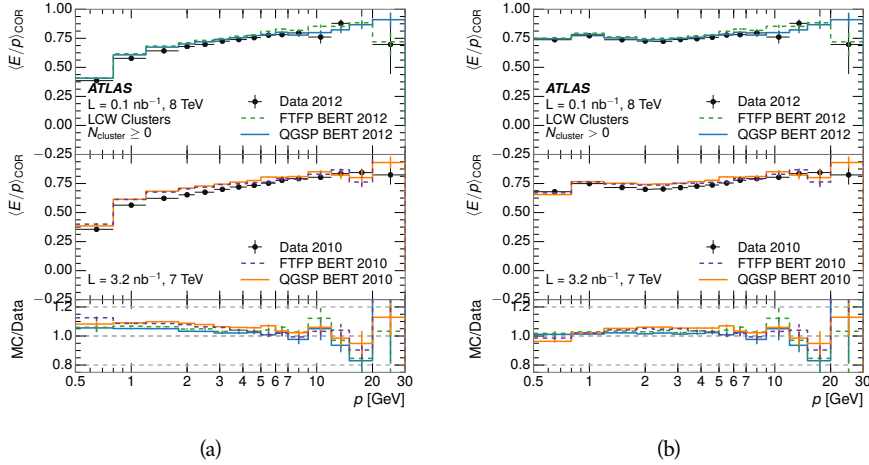


Figure 7:  $\langle E/p \rangle_{\text{COR}}$  calculated using LCW-calibrated topological clusters as a function of track momentum for tracks with (a) zero or more associated topological clusters or (b) one or more associated topological clusters.

#### 552 8.2.41 ADDITIONAL STUDIES

553 As has been seen in several previous measurements, the simulation does not  
 554 correctly model the chance of a low momentum hadron to reach the calorime-  
 555 ter. Because of the consistent discrepancy across pseudorapidity and interaction  
 556 lengths, this seems to be best explained by incomplete understanding of hadronic  
 557 interactions with the detector. For example, a hadron that scatters off of a nu-  
 558 cleus in the inner detector can be deflected through a significant angle and not  
 559 reach the expected location in the calorimeter. In addition, these interactions can  
 560 produce secondary particles that are difficult to model.

561 The requirement on the number of hits in the TRT reduces these effects by  
 562 preferentially selecting tracks that do not undergo nuclear interactions. It is inter-  
 563 esting to check how well the simulation models tracks with low numbers of  
 564 TRT hits, where the nuclear interactions are much more likely. Figure 8 com-  
 565 pares the distributions with  $N_{\text{TRT}} < 20$  to  $N_{\text{TRT}} > 20$  for real and simulated  
 566 particles. As expected, the tracks with fewer hits are poorly modeled in the sim-  
 567 ulation as  $\langle E/p \rangle_{\text{COR}}$  differs by as much as 25% at low momentum.

568 Another interesting aspect of the simulation is the description of antiprotons  
 569 at low momentum, where QGSP\_BERT and FTFP\_BERT have significant differ-  
 570 ences. This can be seen to have an effect in the inclusive response measurement

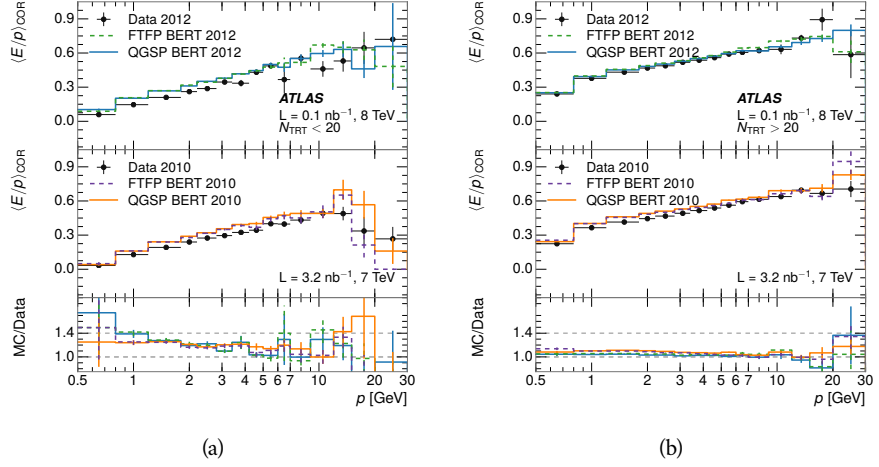


Figure 8: Comparison of the  $\langle E/p \rangle_{\text{COR}}$  for tracks with (a) less than and (b) greater than 20 hits in the TRT.

when separated into positive and negative charge. The  $\langle E/p \rangle_{\text{COR}}$  distributions for positive and negative particles are shown in Figure 9, where a small difference between QGSP\_BERT and FTFP\_BERT can be seen in the distribution for negative tracks. This is demonstrated more clearly in Figure 10, which shows the  $E/p$  distribution in the two simulations separated by charge. There is a clear difference around  $E/p > 1.0$ , which can be explained by the additional energy deposited by the annihilation of the antiproton in the calorimeter that is modeled well only in FTFP\_BERT. This is also explored with data using identified antiprotons in Section 8.3.

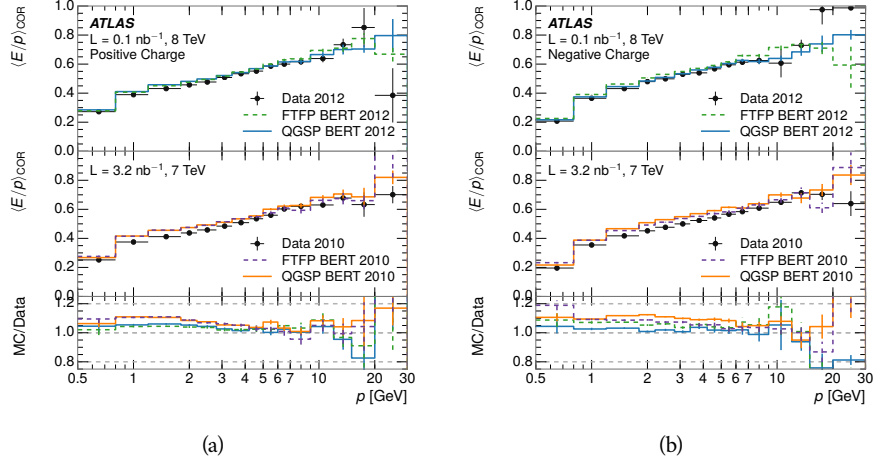


Figure 9: Comparison of the  $\langle E/p \rangle_{\text{COR}}$  for (a) positive and (b) negative tracks as a function of track momentum for tracks with  $|\eta| < 0.6$ .

The  $\langle E/p \rangle$  results in previous sections have considered the electromagnetic and hadronic calorimeters together as a single energy measurement, to emphasize the total energy deposited for a given particle. However, the deposits in each

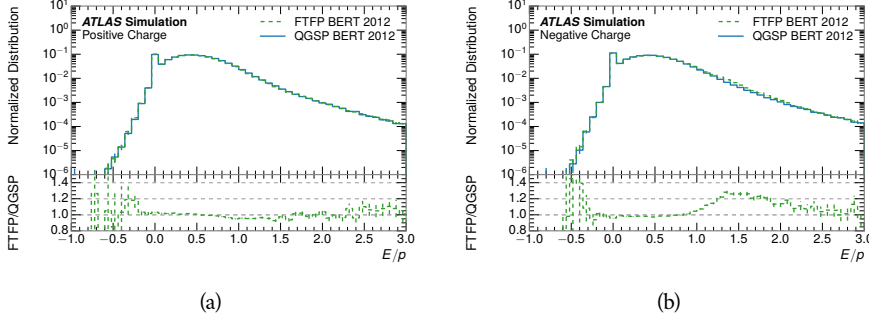


Figure 10: Comparison of the  $E/p$  distributions for (a) positive and (b) negative tracks with  $0.8 < p/\text{GeV} < 1.2$  and  $|\eta| < 0.6$ , in simulation with the FTFP\_BERT and QGSP\_BERT physics lists.

583 calorimeter are available separately and  $\langle E/p \rangle$  can be constructed for each layer.  
 584 As the layers are composed of different materials and are modeled separately in  
 585 the detector geometry, confirmation that the simulation matches the data well  
 586 in each layer adds confidence in both the description of hadronic interactions  
 587 with the two different materials and also the geometric description of each.

588 The technique discussed in Section 8.2.3 for selecting minimally ionizing par-  
 589 ticle (**MIP**s) in the electromagnetic calorimeter is also useful in studying deposits  
 590 in the hadronic calorimeter. Those **MIP**s deposit almost all of their energy ex-  
 591 clusively in the hadronic calorimeter. Figure 11 shows  $\langle E/p \rangle_{\text{RAW}}^{\text{Had}}$ , where RAW  
 592 indicates that no correction has been applied for neutral backgrounds and Had  
 593 indicates that only clusters for the hadronic calorimeter are included. The RAW  
 594 and COR versions of  $\langle E/p \rangle$  in this case are the same, as the neutral background  
 595 is negligible in that calorimeter layer. The distributions are shown both for the  
 596 original EM scale calibration and after LCW calibration. The data and simulation  
 597 agree very well in this comparison, except in the lowest momentum bin which  
 598 has 5% discrepancy that has already been seen in similar measurements.

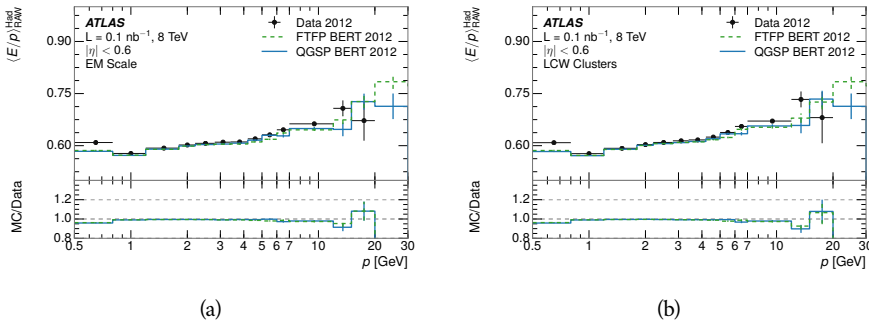


Figure 11: Comparison of the response of the hadronic calorimeter as a function of track momentum (a) at the EM-scale and (b) after the LCW calibration.

599 A similar comparison can be made in the electromagnetic calorimeter by se-  
 600 lecting particles which have no associated energy in the hadronic calorimeter.  
 601 These results are measured in terms of  $\langle E/p \rangle_{\text{COR}}^{\text{EM}}$ , where EM designates that

602 only clusters in the electromagnetic calorimeter are included and COR designates that the neutral background is subtracted as the neutral background is  
 603 present in this case. Figure 12 shows the analogous comparisons to Figure 11 in  
 604 the electromagnetic calorimeter. In this case the disagreement between data and  
 605 simulation is more pronounced, with discrepancies as high as 5% over a larger  
 606 range of momenta. This level of discrepancy indicates that the description of the  
 607 electromagnetic calorimeter is actually the dominant source of discrepancy in  
 608 the combined distributions in Section 8.2.4.  
 609

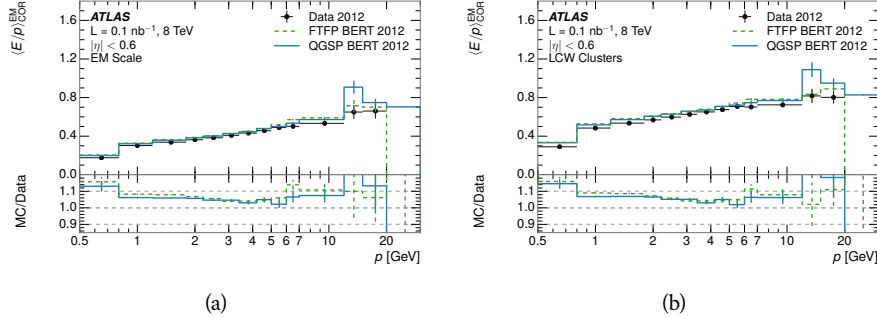


Figure 12: Comparison of the response of the EM calorimeter as a function of track momentum (a) at the EM-scale and (b) with the LCW calibration.

610 **NOTE: There are more studies that I skipped for brevity that could be**  
 611 **included if interesting. E/p at different cluster threshold settings, E/p with**  
 612 **pileup, E/p with cells. I also left out a lot of eta bins that appear in the paper**  
 613 **so that this section didn't turn into 20 pages of plots.**

### 614 8.3 IDENTIFIED PARTICLE RESPONSE

615 The inclusive response measurement for hadrons can be augmented by measuring  
 616 the response for specific particle species. The simulation models each parti-  
 617 cle type separately, and understanding the properties of each is important in con-  
 618 straining the uncertainty on jets. In order to select and measure specific hadrons,  
 619 this section relies on the displaced decays of long-lived particles. Such decays can  
 620 be identified by reconstructing secondary vertices with a requirement on mass.  
 621 In particular,  $\Lambda$ ,  $\bar{\Lambda}$ , and  $K_S^0$  can be used to select a pure sample of protons, an-  
 622 tiprotons, and pions, respectively.

#### 623 8.3.1 DECAY RECONSTRUCTION

624 The measurement of response for identified particles uses the same selection  
 625 as for inclusive particles (Section 8.1.3) with a few additions. Each event used  
 626 is required to have at least one secondary vertex, and the tracks are required  
 627 to match to that vertex rather than the primary vertex. Pions are selected from  
 628 decays of  $K_S^0 \rightarrow \pi^+ \pi^-$ , which is the dominant decay for  $K_S^0$  to charged particles.  
 629 Protons are selected from decays of  $\Lambda \rightarrow \pi^- p$  and antiprotons from  $\bar{\Lambda} \rightarrow \pi^+ \bar{p}$ ,

which are similarly the dominant decays of  $\Lambda$  and  $\bar{\Lambda}$  to charged particles. The species of parent hadron in these decays is determined by reconstructing the mass of the tracks associated to the secondary vertex. The sign of the higher momentum decay particle can distinguish between  $\Lambda$  and  $\bar{\Lambda}$ , which of course have the same mass, as the proton or antiproton is kinematically favored to have higher momentum. Examples of the reconstructed masses used to select these decays are shown in Figure 13.

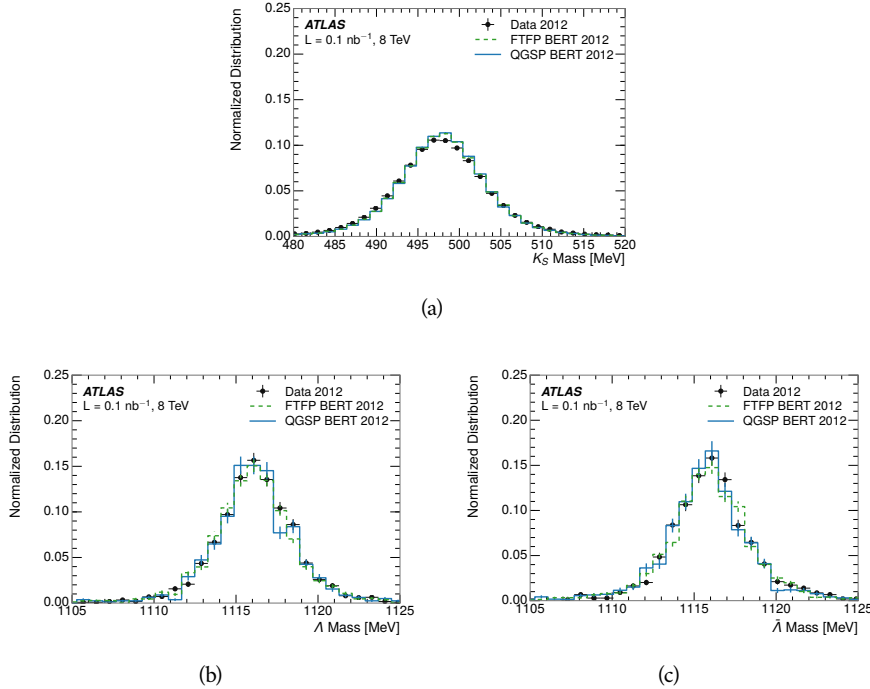


Figure 13: The reconstructed mass peaks of (a)  $K_S^0$ , (b)  $\Lambda$ , and (c)  $\bar{\Lambda}$  candidates.

The dominant backgrounds for the identified particle decays are nuclear interactions and combinatoric sources. These are suppressed by the kinematic requirements on the tracks as well as an additional veto which removes candidates that are consistent with both a  $\Lambda$  or  $\bar{\Lambda}$  and a  $K_S^0$  hypothesis, which is possible because of the different assumptions on particle mass in each case [5]. After these requirements, the backgrounds are found to be negligible compared to the statistical errors on these measurements.

### 8.3.2 IDENTIFIED RESPONSE

With these techniques the  $E/p$  distributions are extracted in data and simulation for each particle species and shown in Figure 14. These distributions are shown for a particular bin of  $E_a$  ( $2.2 < E_a/\text{GeV} < 2.8$ ), rather than  $p$ .  $E_a$  is the energy available to be deposited in the calorimeter: for pions  $E_a = \sqrt{p^2 + m^2}$ , for protons  $E_a = \sqrt{p^2 + m^2} - m$ , and for antiprotons  $E_a = \sqrt{p^2 + m^2} + m$ . The features of the  $E/p$  distributions are similar to the inclusive case. There is a small negative tail from noise and a large fraction of tracks with zero energy from particles which do not reach the calorimeter. The long positive tail is noticeably more

653 pronounced for antiprotons because of the additional energy generated by the  
 654 annihilation in addition to the neutral background.

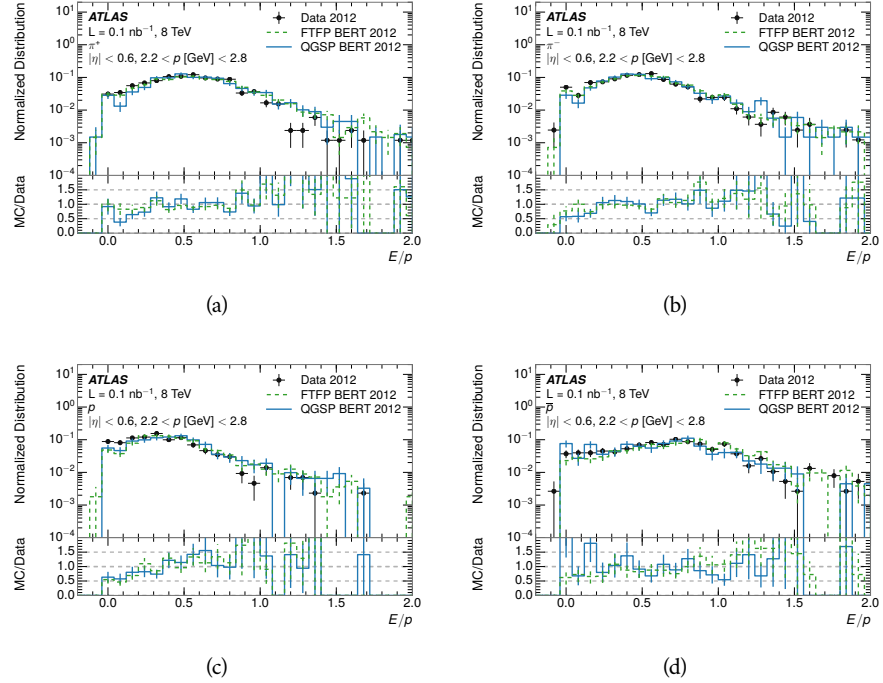


Figure 14: The  $E/p$  distribution for isolated (a)  $\pi^+$ , (b)  $\pi^-$ , (c) proton, and (d) anti-proton tracks.

655 The zero fraction is further explored in Figure 15 for pions and protons in  
 656 data and simulation. The simulation consistently underestimates the zero frac-  
 657 tion independent of particle species, which implies that this discrepancy is not  
 658 caused by the model of a particular species but rather a feature common to all.

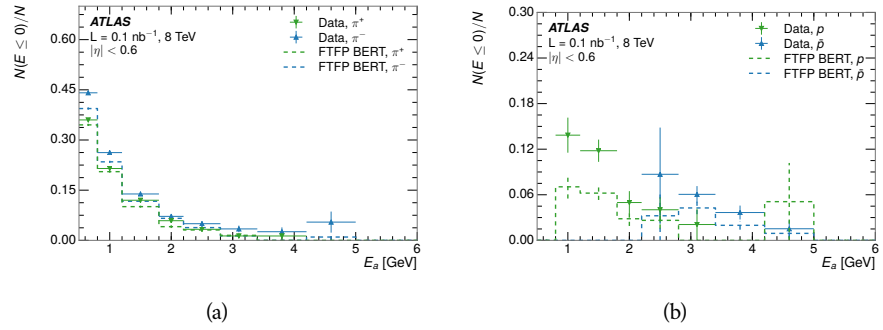


Figure 15: The fraction of tracks with  $E \leq 0$  for identified (a)  $\pi^+$  and  $\pi^-$ , and (b) proton and anti-proton tracks

659 It is also interesting to compare the response between the different particle  
 660 species. One approach to do this is to measure the difference in  $\langle E/p \rangle$  between  
 661 two types, which has the advantage of removing the neutral background. These  
 662 differences are shown in various combinations in Figure 16. The response for

$\pi^+$  is greater on average than the response to  $\pi^-$  because of a charge-exchange effect which causes the production of additional neutral pions in the showers of  $\pi^+$  [20]. The response for  $\pi^+$  is also greater on average than the response to  $p$ , because a large fraction of the energy of  $\pi^+$  hadrons is converted to an electromagnetic shower [11, 25]. However, the  $\bar{p}$  response is significantly higher than the response to  $\pi^-$  because of the annihilation of the antiproton. FTFP\_BERT does a better job of modeling this effect than QGSP\_BERT because of their different descriptions of  $\bar{p}$  interactions with material.

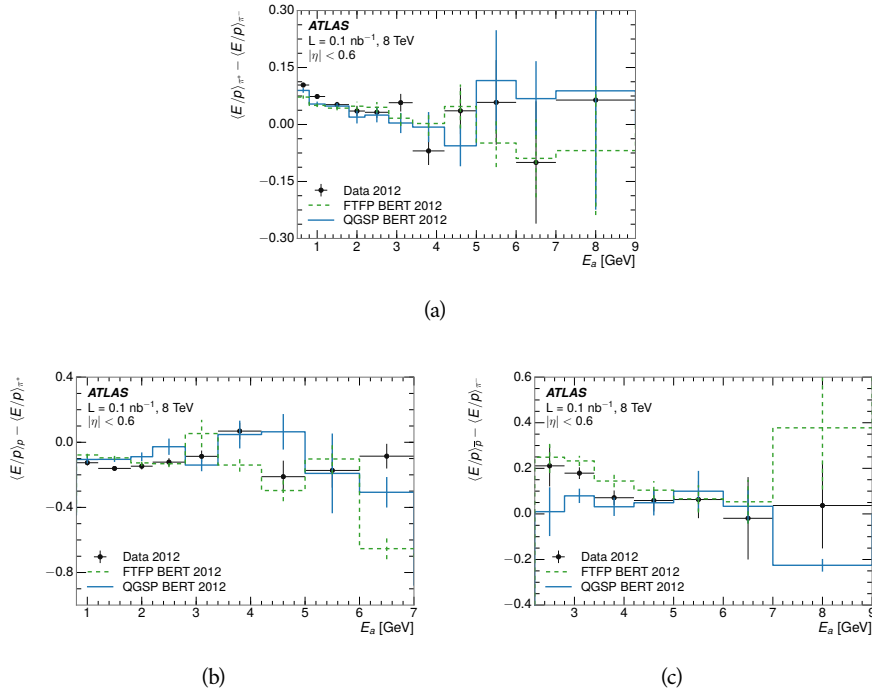


Figure 16: The difference in  $\langle E/p \rangle$  between (a)  $\pi^+$  and  $\pi^-$  (b)  $p$  and  $\pi^+$ , and (c)  $\bar{p}$  and  $\pi^-$ .

It is also possible to remove the neutral background from these response distributions using the same technique as in Section 8.2.3. The technique is largely independent of the particle species and so can be directly applied to  $\langle E/p \rangle$  for pions. The  $\langle E/p \rangle_{\text{COR}}$  distributions for pions are shown in Figure 17, which are very similar to the inclusive results. The inclusive hadrons are comprised mostly of pions, so this similarity is not surprising. It is also possible to see the small differences between  $\pi^+$  and  $\pi^-$  response here, where  $\langle E/p \rangle_{\text{COR}}$  is higher on average for  $\pi^+$ . The agreement between data and simulation is significantly worse for the  $\pi^-$  distributions than for the  $\pi^+$ , with a discrepancy greater than 10% below 2-3 GeV.

### 8.3.3 ADDITIONAL SPECIES IN SIMULATION

The techniques above provide a method to measure the response separately for only pions and protons. However the hadrons which forms jets include a number of additional species such as kaons and neutrons. The charged kaons are

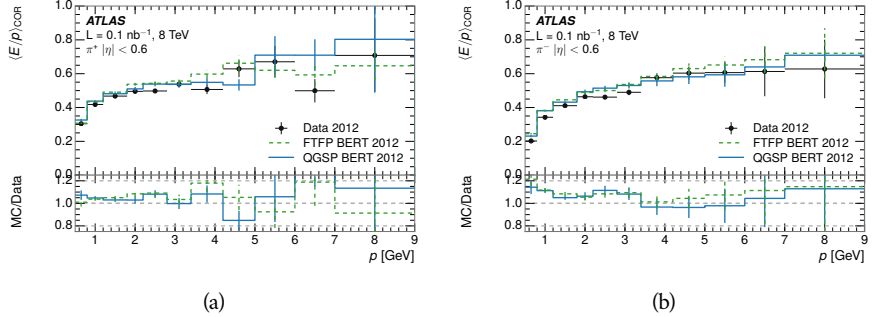


Figure 17:  $\langle E/p \rangle_{\text{COR}}$  as a function of track momentum for (a)  $\pi^+$  tracks and (b)  $\pi^-$  tracks.

685 an important component of the inclusive charged hadron distribution, which is  
 686 comprised of roughly 60-70% pions, 15-20% kaons, and 5-15% protons. These  
 687 are difficult to measure in data at the ATLAS detector, although a template sub-  
 688 traction technique has been proposed which may be effective with larger sam-  
 689 ple sizes [8]. The simulation of these particles includes noticeable differences in  
 690 response at low energies, which are shown in Figure 18 for FTFP\_BERT. The  
 691 significant differences in response between low energy protons and antiprotons  
 692 are accounted for above in the definitions of  $E_a$ .

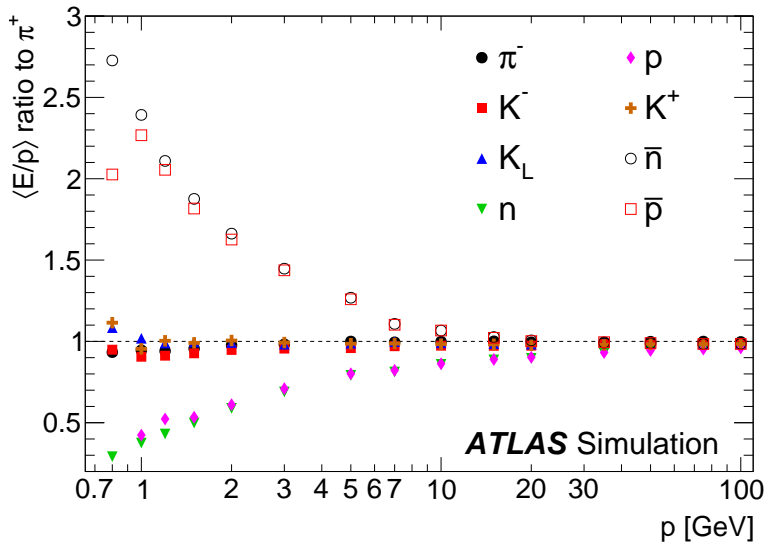


Figure 18: The ratio of the calorimeter response to single particles of various species to the calorimeter response to  $\pi^+$  with the physics list FTFP\_BERT.

693 8.4 SUMMARY

These various measurements of calorimeter response shown above for data and simulation illuminate the accuracy of the simulation of hadronic interactions at the ATLAS detector. The results were done using 2010 and 2012 data at 7 and 8

697 TeV, but reflect the most current understanding of the detector alignment and  
698 geometry. A number of measurements focusing on a comparison between pro-  
699 tons and antiprotons suggest that FTFP\_BERT models those interaction more  
700 accurately than QGSP\_BERT. These measurements, among others, were the moti-  
701 vation to switch the default Geant4 simulation from FTFP\_BERT to QGSP\_BERT  
702 for all ATLAS samples.

703 Even with these updates, there are a number of small, approximately 5%, dis-  
704 crepancies in response between the data and simulation at low energies. At higher  
705 energies the simulation of hadronic interactions is very consistent with data.  
706 Chapter 9 discusses how to use these observed differences to constrain the jet  
707 energy scale and its associated uncertainties.



708

## 709 JET ENERGY RESPONSE AND UNCERTAINTY

## 710 9.1 MOTIVATION

711 As jets form a major component of many physics analyses at ATLAS, it is cru-  
 712 cial to carefully calibrate the measurement of jet energies and to derive an un-  
 713 certainty on that measurement. These uncertainties have often been the domi-  
 714 nant systematic uncertainty in high-energy analyses at the Large Hadron Col-  
 715 llider ([LHC](#)). Dijet and multijet balance techniques provide a method to constrain  
 716 the [JES](#) and its uncertainty in data, and provide the default values used for ATLAS  
 717 jet measurements at most energies [7]. These techniques are limited by their re-  
 718 liance on measuring jets in data, so they are statistically limited in estimating  
 719 the jet energy scale at the highest jet energies. This chapter presents another  
 720 method for estimating the jet energy scale and its uncertainty which builds up a  
 721 jet from its components and thus can be naturally extended to high jet momen-  
 722 tum. Throughout this chapter the jets studied are simulated using [Pythia8](#) with  
 723 the CT10 parton distribution set [27] and the AU2 tune [3], and corrections are  
 724 taken from the studies including data and simulation in Chapter 8.

725 As described in Section 7.2, jets are formed from topological clusters of energy  
 726 in the calorimeters using the anti- $k_t$  algorithm. These clusters originate from a  
 727 diverse spectrum of particles, in terms of both species and momentum, leading to  
 728 significantly varied jet properties and response between jets of similar produced  
 729 momentum. Figure 19 shows the simulated distribution of particles within jets  
 730 at a few examples energies. The  $E/p$  measurements provide a thorough under-  
 731 standing of the dominant particle content of jets, the charged hadrons.

## 732 9.2 UNCERTAINTY ESTIMATE

733 Simulated jets are not necessarily expected to correctly model the energy de-  
 734 posits in the calorimeters, because of the various discrepancies discussed in Chap-  
 735 ter 8. To evaluate a jet energy response, the simulated jet energies are compared  
 736 to a corrected jet built up at the particle level. Each cluster in a jet is associated  
 737 to the truth particle which deposited it, and the energy in that cluster is then  
 738 corrected for a number of effects based on measurements in data. The primary  
 739 corrections come from the single hadron response measurements in addition to  
 740 response measured using the combined test beam which covers higher momen-  
 741 tum particles [10]. These corrections include both a shift ( $\Delta$ ), in order to make the  
 742 simulation match the average response in data, and an uncertainty ( $\sigma$ ) associated  
 743 with the ability to constrain the difference between data and simulation. Some of  
 744 the dominant sources of uncertainty are itemized in Table ?? with typical values,  
 745 and the full list considered is described in detail in the associated paper [8]. These

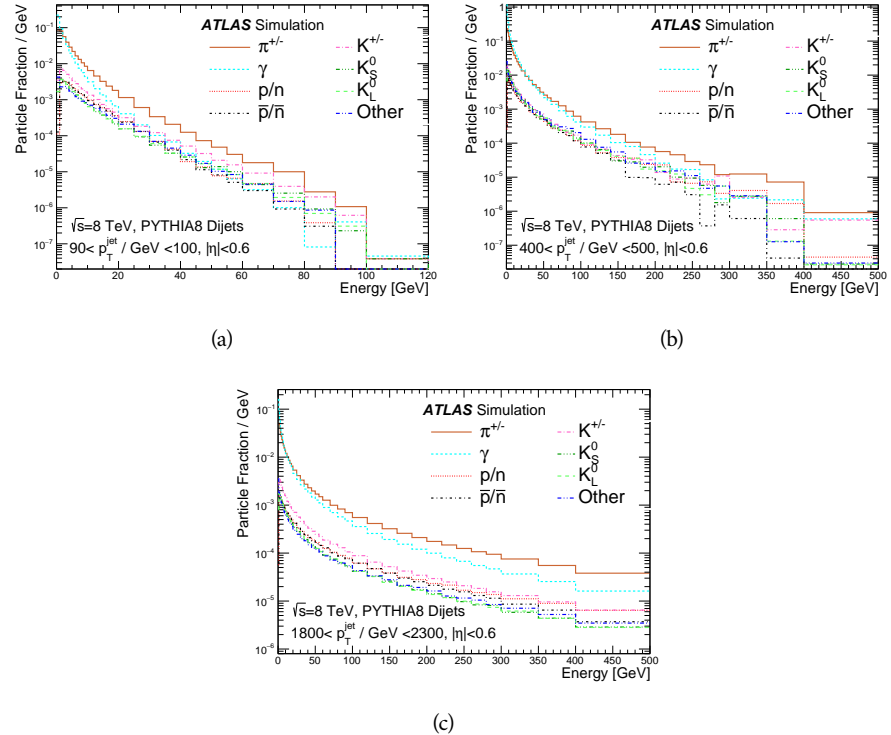


Figure 19: The spectra of true particles inside anti- $k_t$ ,  $R = 0.4$  jets with (a)  $90 < p_T/\text{GeV} < 100$ , (b)  $400 < p_T/\text{GeV} < 500$ , and (c)  $1800 < p_T/\text{GeV} < 2300$ .

746 uncertainties cover differences between the data and simulation in the modeling  
 747 of calorimeter response to a given particle. No uncertainties are added for the  
 748 difference between particle composition of jets in data and simulation.

749 From these terms, the jet energy scale and uncertainty is built up from individual  
 750 energy deposits in simulation. Each uncertainty term is treated independently,  
 751 and are taken to be gaussian distributed. The resulting scale and uncertainty  
 752 is shown in Figure 20, where the mean response is measured relative to  
 753 the calibrated energy reported by simulation. The dominant uncertainties come  
 754 from the statistical uncertainties on the  $E/p$  measurements at lower energies and  
 755 the additional uncertainty for out of range measurements at higher energies. The  
 756 total uncertainty from this method at intermediate jet energies is comparable to  
 757 other simulation-based methods [4] and is about twice as large as in-situ methods  
 758 using data [7]. This method is the only one which provides an estimation  
 759 above 1.8 TeV, however, and so is still a crucial technique in analyses that search  
 760 for very energetic jets.

761 These techniques can also be used to measure the correlation between bins of  
 762 average reconstructed jet momentum across a range of  $p_T$  and  $|\eta|$ , where cor-  
 763 relations are expected because of a similarity in particle composition at similar  
 764 energies. Figure 21 shows these correlations, where the uncertainties on jets in  
 765 neighboring bins are typically between 30% and 60% correlated. The uncertainty  
 766 on all jets becomes significantly correlated at high energies and larger pseudora-

Abbrev.	Description	$\Delta$ (%)	$\sigma$ (%)
In situ $E/p$	The comparison of $\langle E/p \rangle_{\text{COR}}$ as described in Chapter 8 with statistical uncertainties from 500 MeV to 20 GeV.	0-3	1-5
CTB	The main $\langle E/p \rangle$ comparison uncertainties, binned in $p$ and $ \eta $ , as derived from the combined test beam results, from 20 to 350 GeV [10].	0-3	1-5
$E/p$ Zero Fraction	The difference in the zero-fraction between data and MC simulation from 500 MeV to 20 GeV.	5-25	1-5
$E/p$ Threshold	The uncertainty in the EM calorimeter response from the potential mismodeling of threshold effects in topological clustering.	0	0-10
Neutral	The uncertainty in the calorimeter response to neutral hadrons based on studies of physics model variations.	0	5-10
$K_L$	An additional uncertainty in the response to neutral $K_L$ in the calorimeter based on studies of physics model variations.	0	20
$E/p$ Misalignment	The uncertainty in the $p$ measurement from misalignment of the ID.	0	1
Hadrons, $p > 350$ GeV	A flat uncertainty for all particles above the energy range or outside the longitudinal range probed with the combined test beam.	0	10

Table 1: The dominant sources of corrections and systematic uncertainties in the [JES](#) estimation technique, including typical values for the correcting shift ( $\Delta$ ) and the associated uncertainty ( $\sigma$ ).

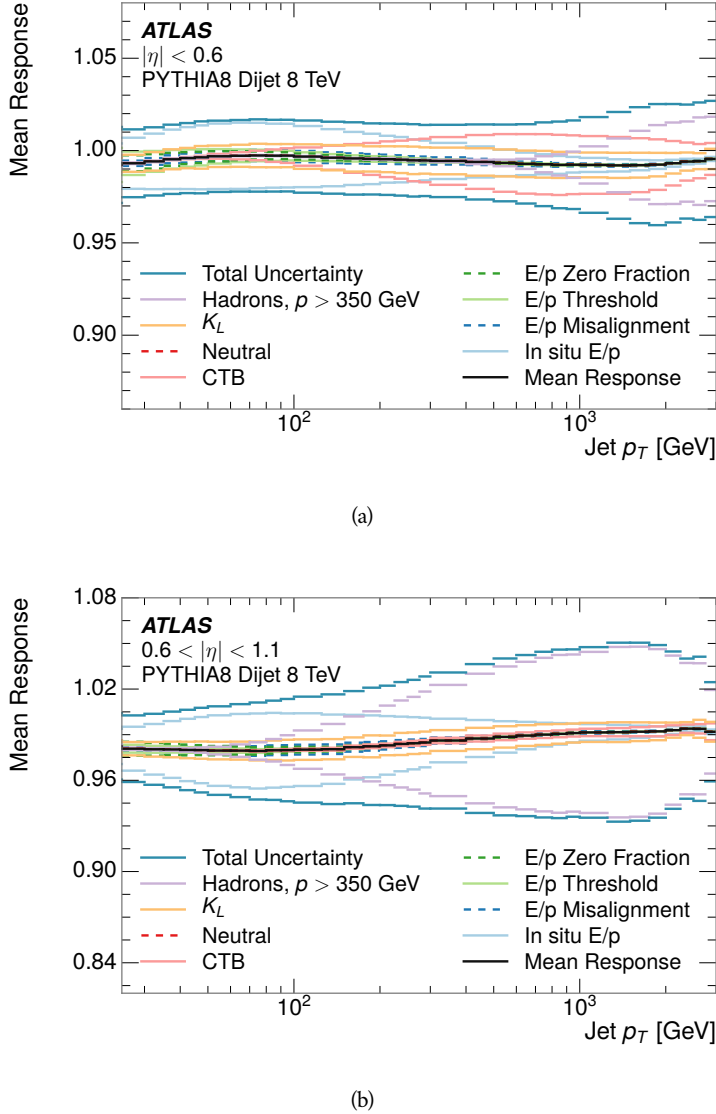


Figure 20: The `JES` uncertainty contributions, as well as the total `JES` uncertainty, as a function of jet  $p_T$  for (a)  $|\eta| < 0.6$  and (b)  $0.6 < |\eta| < 1.1$ .

767      pilities, when the uncertainty becomes dominated by the single term reflecting  
 768      out of range particles.

### 769      9.3 SUMMARY

770      The technique described above provides a jet energy scale and uncertainty by  
 771      building up jet corrections from the energy deposits of constituent particles. The  
 772       $E/p$  measurements are crucial in providing corrections for the majority of parti-  
 773      cles in the jets. The uncertainty derived this way is between 2 and 5% and is about  
 774      twice as large at corresponding momentum than jet balance methods. However  
 775      this is the only uncertainty available for very energetic jets using 2012 data and  
 776      simulation, and repeating this method with Run 2 data and simulation will be

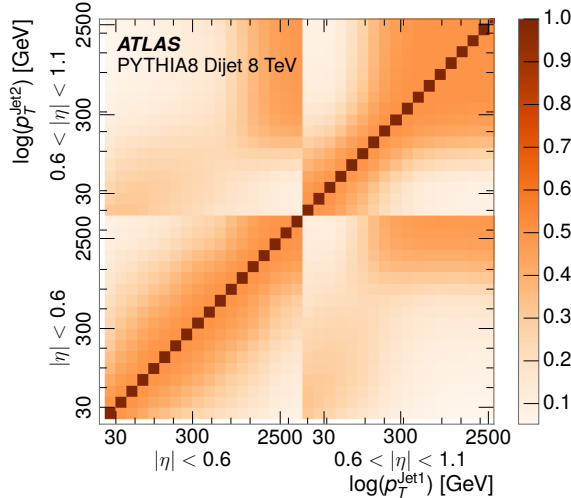


Figure 21: The JES correlations as a function of jet  $p_T$  and  $|\eta|$  for jets in the central region of the detector.

777 important in providing an uncertainty for the most energetic jets in 13 TeV col-  
778 lisions.



779

## PART V

780

### SEARCH FOR LONG-LIVED PARTICLES

781

You can put some informational part preamble text here.



# 10

782

783 LONG-LIVED PARTICLES IN ATLAS

---

784 10.1 OVERVIEW AND CHARACTERISTICS

785 10.2 SIMULATION



787 EVENT SELECTION

---

788 The Long-Lived Particles ([LLPs](#)) targeted by this search differ in their interactions  
 789 with the detector from [SM](#) particles primarily because of their large mass. When  
 790 produced at the energies available at the [LHC](#), that large mass results in a low  $\beta$   
 791 and such slow-moving particles heavily ionize in detector material. Each layer  
 792 of the pixel detector provides a measurement of that ionization, through time  
 793 over threshold ([ToT](#)), as discussed in Section [6.3.1](#). The ionization in the pixel  
 794 detector, quantified in terms of  $dE/dx$ , provides the major focus for this search  
 795 technique, both for its discriminating power and also because of the large range  
 796 of lifetimes where it can be used. The  $dE/dx$  variable needs to be augmented  
 797 with a few additional selection requirements to form a complete search.

798 Ionization is not currently available in any form during triggering, so this  
 799 search instead relies on  $E_T^{\text{miss}}$  to trigger signal events. Although triggering on  
 800  $E_T^{\text{miss}}$  is not particularly efficient,  $E_T^{\text{miss}}$  is often large for many production mech-  
 801 anisms of [LLPs](#), as discussed in Section [10.1](#).

802 Ionization is most effective in rejecting backgrounds for well-measured, high-  
 803 momentum tracks, so some basic requirements on quality and kinematics are  
 804 placed on the particles considered in this search. In particular a newly introduced  
 805 tracking variable is very effective in removing highly-ionizing backgrounds caused  
 806 by overlapping tracks. A few additional requirements are placed on the tracks  
 807 considered for [LLP](#) candidates that increase background rejection by targeting  
 808 specific types of [SM](#) particles. These techniques provide a significant analysis  
 809 improvement over previous iterations of ionization-based searches on ATLAS  
 810 by providing additional background rejection with minimal loss in signal effi-  
 811 ciency.

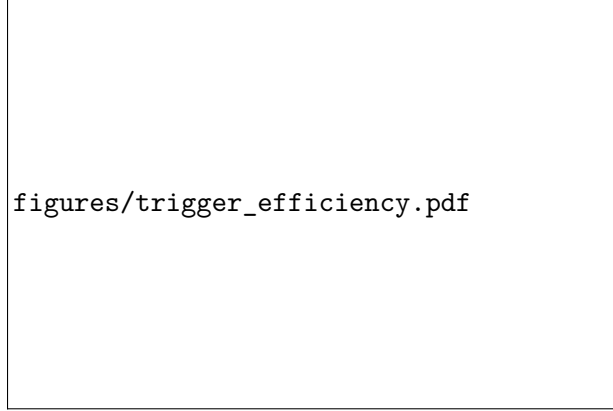
812 The ionization measurement with the Pixel detector can be calibrated to pro-  
 813 vide an estimator of  $\beta\gamma$ . That estimate, together with the momentum measure-  
 814 ment provided by tracking, can be used to reconstruct a mass for each track  
 815 which traverses the pixel detector. That mass variable will be peaked at the [LLP](#)  
 816 mass for any signal, and provides an additional tool to search for an excess. In  
 817 addition to an explicit requirement on ionization, this search constructs a mass-  
 818 window for each targeted mass range in order to evaluate any excess of events  
 819 and to set limits.

820 The strategy discussed here is optimized for lifetimes of  $O(1) - O(10)$  ns.  
 821 Pixel ionization is especially useful in this regime as particles only need to prop-  
 822 agate through the first seven layers of the inner detector, about 37 cm from the  
 823 beam axis. The search is still competitive with other searches for [LLPs](#) at longer  
 824 lifetimes, because the primary discriminating variables are still applicable even  
 825 for particles that do not decay within the detector. Although the basic strategy  
 826 remains the same for all lifetimes, two signal regions are defined to optimize  
 827 separately for intermediate and long lifetime particles.

## 828 11.1 TRIGGER

829 Triggering remains one of the primary difficulties in defining an event selection  
 830 with high signal efficiency in a search for **LLPs**. There are no triggers available in  
 831 the current ATLAS system that can fire directly from a high momentum track  
 832 with large ionization (Section 6.6). Although in some configurations a charged  
 833 **LLP** can fire muon triggers, this requirement introduces significant model depen-  
 834 dence on both the allowed lifetimes and the interactions in the calorimeter.

835 For a search targetting particles which may decay prior to reaching the muon  
 836 system, the most efficient available trigger is based on missing energy. As dis-  
 837 cussed in Section 10.1, signal events can produce  $E_T^{\text{miss}}$  by two primary mech-  
 838 anisms. The decays of R-Hadrons to neutralinos can produce missing energy  
 839 when the neutralinos go undetected in the calorimeters. **LLPs** which do not de-  
 840 cay before the calorimeters also can produce missing energy because they do  
 841 not deposit much energy. Either case to some extent relies on kinematic degrees  
 842 of freedom to produce missing energy, as the pair-produced **LLPs** tend to bal-  
 843 ance each other in the transverse plain. That balance results in a relatively low  
 844 efficiency for long-lifetime particles, roughly 40%, and efficiencies between 65%  
 845 and 95% for shorter lifetimes depending on both the mass and the lifetime, as  
 846 seen in Figure 22.



figures/trigger\_efficiency.pdf

Figure 22: The trigger efficiency of the  $E_T^{\text{miss}}$  trigger as a function of mass and lifetime.

## 847 11.2 KINEMATICS AND ISOLATION

848 After the trigger requirement, each event is required to have a primary vertex  
 849 reconstructed from at least two well-measured tracks in the inner detector, each  
 850 with  $p_T > 400$  MeV. If more than one such vertex exists, the primary vertex is  
 851 taken to be the one with the largest summed track momentum for all tracks as-  
 852 sociated to that vertex. The offline reconstructed  $E_T^{\text{miss}}$  is required to be above  
 853 130 GeV to additionally reject **SM** backgrounds. The transverse missing energy  
 854 is calculated using fully reconstructed and calibrated offline objects, as described  
 855 in Section 7.5. In particular the  $E_T^{\text{miss}}$  definition in this selection uses jets recon-  
 856 structed with the anti- $k_t$  algorithm with radius  $R = 0.4$  from clusters of energy

857 in the calorimeter (Section 7.2) and with  $p_T > 20$  GeV, as well as reconstructed  
 858 muons, electrons, and tracks not identified as another object type.

859 The  $E_T^{\text{miss}}$  distributions are shown for data and a few simulated signals in Fig-  
 860 ure 23, after the trigger requirement. The cut placed at 130 GeV is 95% efficient  
 861 for metastable and 90% efficient for stable particles, because of the missing en-  
 862 ergy generating mechanisms discussed previously. The distribution of data in  
 863 this figure and subsequent figures in this section can be interpreted as the dis-  
 864 tribution of backgrounds, as any signal contamination would be negligible if  
 865 present at these early stages of the selection (prior to the final requirement on  
 866 mass). The background falls rapidly with missing energy, motivating the direct  
 867 requirement on  $E_T^{\text{miss}}$  for the signal region. Although a higher requirement than  
 868 the specified value of 130 GeV would seem to increase the search potential from  
 869 these early distributions, other requirements are more optimal when taken as a  
 870 whole. The specific values for each requirement in signal region were optimized  
 871 considering the increase in discovery reach for tightening the requirement on  
 872 each discriminating variable. **NOTE: Is it interesting to discuss the signal re-**  
 873 **gion optimization process in detail? I could add another section on how**  
 874 **the values were determined, although in truth it is at least partially his-**  
 875 **torical precedence.**

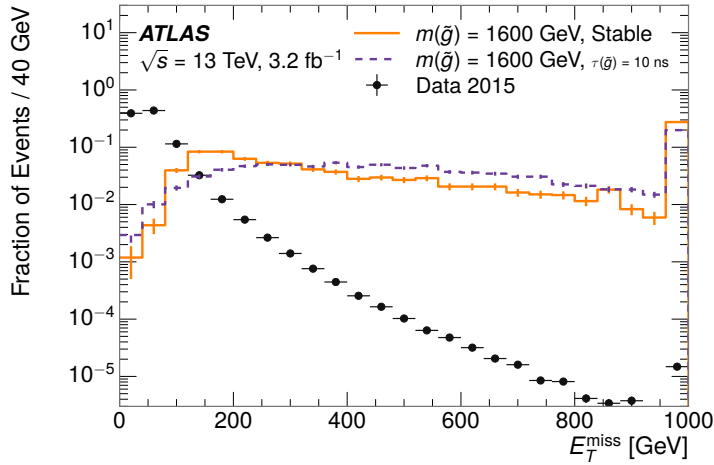


Figure 23: The distribution of  $E_T^{\text{miss}}$  for data and simulated signal events, after the trigger requirement.

876 Potential signal events are then required to have at least one candidate [LLP](#)  
 877 track. Although the [LLPs](#) are produced in pairs, many models do not consistently  
 878 yield two charged particles. For example, in the R-Hadron model highlighted  
 879 here, only 20% of events have two charged R-Hadrons while 47% of events have  
 880 just one. A signal region requiring two charged candidates could be a powerful  
 881 improvement in background rejection for a larger dataset, but it is not consid-  
 882 ered in this version of the analysis as it was found to be unnecessary to reject the  
 883 majority of backgrounds.

884 For a track to be selected as a candidate, it must have  $p_T > 50$  GeV and pass  
 885 basic quality requirements. The track must be associated to the primary vertex. It

886 must also have at least seven clusters in the silicon layers in the inner detector to  
 887 ensure an accurate measurement of momentum. Those clusters must include one  
 888 in the innermost layer if the extrapolated track is expected to pass through that  
 889 layer. And to ensure a reliable measurement of ionization, the track is required  
 890 to have at least two clusters in the pixel detector that provide a measurement of  
 891  $dE/dx$ .

892 At this point in the selection, there is a significant high-ionization background  
 893 from multiple tracks that significantly overlap in the inner detector. Previous  
 894 version of this analysis have rejected these overlaps by an explicit overlap rejec-  
 895 tion between pairs of fully reconstructed tracks, typically by requiring no addi-  
 896 tional tracks within a cone around the candidate. This technique, however, fails  
 897 to remove the background from tracks that overlap so precisely that the tracks  
 898 cannot be separately resolved.

899 A new method, added in Run 2, identifies cluster shapes that are likely formed  
 900 by multiple tracks based on a neural network classification algorithm. The num-  
 901 ber of clusters that are classified this way in the pixel detector for a given track  
 902 is called  $N_{\text{split}}$ . As the shape of clusters requires significantly less spatial sepa-  
 903 ration to identify overlaps than it does to reconstruct two fully resolved tracks,  
 904 this variable is more effective at rejecting backgrounds from overlaps. Figure 24  
 905 shows the dependence of ionization on  $N_{\text{split}}$ ; as  $N_{\text{split}}$  increases the mean of  
 906  $dE/dx$  grows significantly up to twice the expected value when  $N_{\text{split}} = 4$ .

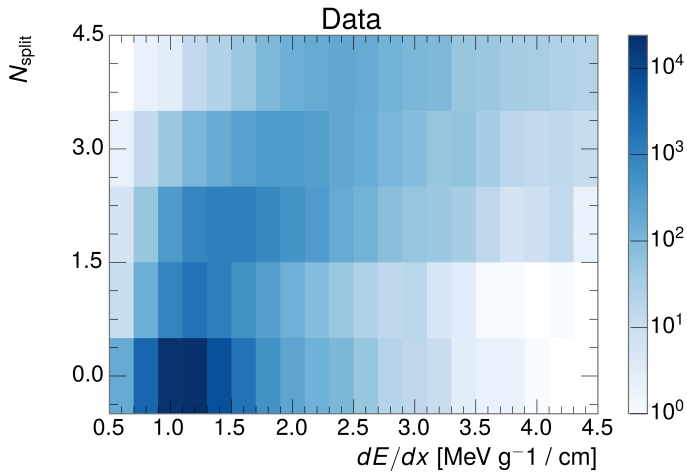


Figure 24: The dependence of  $dE/dx$  on  $N_{\text{split}}$  in data after basic track hit requirements  
 have been applied.

907 This requirement is very successful in reducing the long positive tail of the  
 908  $dE/dx$  distributions, as can be seen in Figure 25. Comparing the distribution for  
 909 “baseline tracks”, tracks with only the above requirements on clusters applied and  
 910 before the requirement on  $N_{\text{split}}$ , to the distribution with  $N_{\text{split}} = 0$ , it is clear  
 911 that the fraction of tracks with large  $dE/dx$  is reduced by several orders of mag-  
 912 nitude. The isolated tracks are very close to the  $dE/dx$  distribution of identified  
 913 muons, which are extremely well isolated on average. Figure 25 also includes  
 914 the distribution of  $dE/dx$  in an example signal simulation to demonstrate how

effective  $dE/dx$  is as a discriminating variable with this isolation applied. The background falls rapidly for  $dE/dx > 1.8 \text{ MeV g}^{-1}\text{cm}^2$  while the majority of the signal, approximately 90% depending on the mass, falls above that threshold. Over 90% of [LLP](#) tracks in simulated signal events pass the  $N_{\text{split}}$ -based isolation requirement.

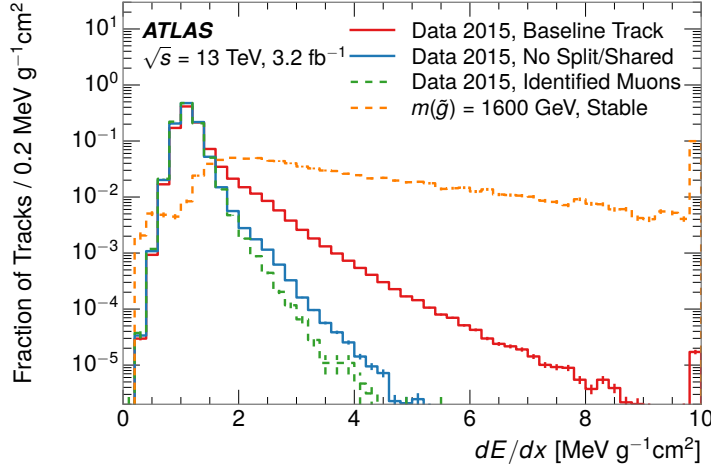


Figure 25: The distribution of  $dE/dx$  with various selections applied in data and simulated signal events.

A few additional kinematic requirements are imposed to help reduce [SM](#) backgrounds. The momentum of the candidate track must be at least 150 GeV, and the uncertainty on that measurement must be less than 50%. The distribution of momentum is shown in Figure 26 for tracks in data and simulated signal events after the previously discussed requirements on clusters, transverse momentum, and isolation have been imposed. The signal particles are much harder on average than their backgrounds because of the high energy interactions required to produce them. The transverse mass,  $m_T$ , defined as

$$m_T = \sqrt{2p_T E_T^{\text{miss}}(1 - \cos(\Delta\phi(E_T^{\text{miss}}, \text{track})))} \quad (1)$$

is required to be greater than 130 GeV to reject contributions from the decay of  $W$  bosons. Figure 27 shows the distribution of  $m_T$  for data and simulated events. **More comments to follow.**

### 11.3 STANDARD MODEL REJECTION

Because the search selects events with just a single, highly-ionizing track, backgrounds can be formed by a wide variety of [SM](#) processes when various charged particles have a few randomly large deposits of energy in the pixel detector. Those backgrounds can be effectively rejected by targeting the types of particles produced rather than the processes which produce them, as [LLPs](#) will have significant differences compared to any [SM](#) particle. These rejections focus on using

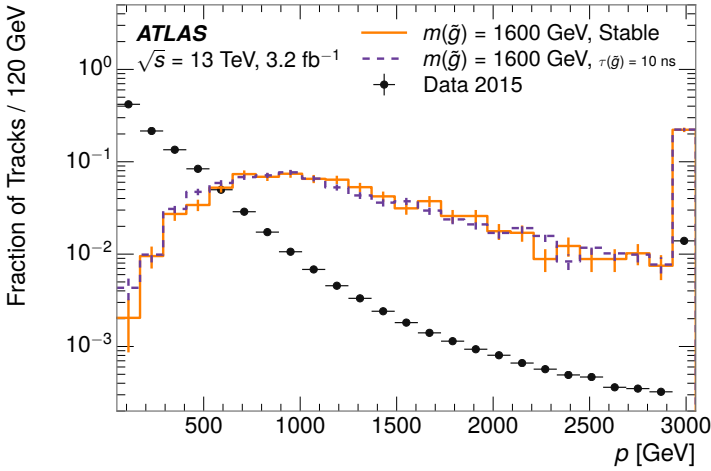


Figure 26: The distribution of track momentum for data and simulated signal events, after previous selection requirements have been applied.

additional features of the event, other than the kinematics or ionization of the candidate track, as it provides a powerful source of background rejection with very high signal efficiency. The lifetime of the particle can significantly change its detector characteristics, as discussed in Section 10.1. To accommodate these differences, the SM rejections defined in this section are split to form two signal regions, one for long-lifetimes particles, the “stable” region, and one for intermediate lifetime particles, the “metastable” region.

Jets can be very effectively rejected by considering the larger-scale isolation of the candidate track. In this case the isolation focuses on the production of nearby particles as a jet-veto, rather than isolation from overlapping tracks to reduce high-ionization backgrounds. As explained in Section 10.1, the fragmentation process which produces an R-Hadron is very hard and thus is not expected to produce additional particles. The jet-veto uses the summed momentum of tracks with a cone of  $\Delta R < 0.25$ , referred to as  $p_T^{\text{Cone}}$ , which is shown in Figure 28 for data and simulated signal events. In the data this value has a peak at zero from isolated tracks such as leptons, and a long tail from jets which contains as much as 80% of the background above 20 GeV at this stage of the selection. In signal events  $p_T^{\text{Cone}}$  is strongly peaked at zero and significantly less than 1% is above 20 GeV. This makes a requirement of  $p_T^{\text{Cone}} < 20$  GeV one of the most effective methods to reject background without losing signal efficiency. For the stable signal region, this cut is further tightened to  $p_T^{\text{Cone}} < 5$  GeV as it is the most effective variable remaining to extend the search reach for long lifetimes.

Even for fully isolated particles, there are additional methods to reject each type of particle using information in the muon system and calorimeters. Muons can be identified very reliably using the tracks in the muon system, as described in Section 7.4. For intermediate lifetimes the LLPs do not survive long enough to reach the muon system, and so muons are vetoed by rejecting tracks that associate to a muon with medium muon identification requirements. For longer



`figures/selection_mt_nm1.pdf`

Figure 27: The distribution of  $M_T$  for data and simulated signal events, after previous selection requirements have been applied.

966 lifetimes, this rejection is not applied because [LLPs](#) which reach the muon system  
 967 can be identified as muons as often as 30% of the time in simulated samples.

968 Calorimeter-based particle rejection relies on the expected small deposits of  
 969 energy from [LLPs](#). When the lifetime is long enough to reach the calorimeter, a  
 970 [LLP](#) deposits little of its energy as it traverses the material, as discussed in Sec-  
 971 tion 10.1. Even when the particle does decay before the calorimeter, the major-  
 972 ity of its energy is carried away by the Lightest Supersymmetric Particle ([LSP](#))  
 973 and not deposited in the calorimeter. In both cases the energy is expected to be  
 974 distributed across the layers of the calorimeters and not peaked in just one layer.  
 975 This can be quantified in terms of  $E/p$ , the ratio of calorimeter energy of a nearby  
 976 jet to the track momentum, and  $f_{EM}$ , the fraction of energy in that jet within  
 977 the electromagnetic calorimeter. When no jets fall within a cone of 0.05 of the  
 978 particle,  $E/p$  and  $f_{EM}$  are both defined as zero.  $E/p$  is expected to be above 1.0  
 979 for typical [SM](#) particles because of calibration and the contributions from other  
 980 nearby particles. At these momenta there is no significant zero fraction due to  
 981 interactions with the detector or insufficient energy deposits (see Section 8.2.2).  
 982  $f_{EM}$  is peaked close to 1.0 for electrons, and distributed between 10% and 90%  
 983 for hadrons.

984 These trends can be seen in the two dimensional distribution for signal in  
 985 Figure 29 for stable and metastable (10 ns) events. The majority of R-Hadrons in  
 986 both samples fall into the bin for  $E/p = 0$  and  $f_{EM} = 0$  because the majority of  
 987 the time there is no associated jet. When there is an associated jet  $E/p$  is typically  
 988 still below 0.1, and the  $f_{EM}$  is predominantly under 0.8. Figure 29 also includes  
 989 simulated Z decays to electrons or tau leptons. From the decays to electrons it is  
 990 clear that the majority of electrons have  $f_{EM}$  above 0.9. The tau decays include a  
 991 variety of products. Muons can be seen in the bin where  $E/p = 0$  and  $f_{EM} = 0$   
 992 because they do not have an associated jet. Electrons fall into the range where  
 993  $E/p > 1$  and  $f_{EM} > 0.9$ . Hadronic tau decays are the most common, and fall in  
 994 the range of  $0.1 < f_{EM} < 0.9$  and  $E/p > 1.0$ .

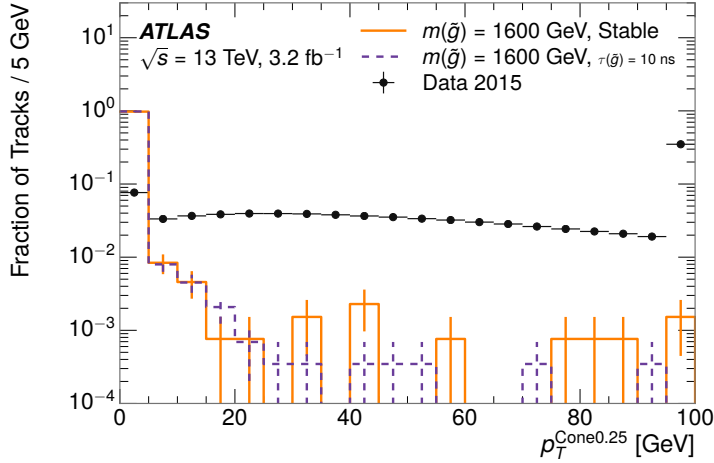


Figure 28: The distribution of summed tracked momentum within a cone of  $\Delta R < 0.25$  around the candidate track for data and simulated signal events, after previous selection requirements have been applied.

995     These differences motivate an electron rejection by requiring an  $f_{\text{EM}}$  below  
 996     0.9. Similarly, isolated hadrons are rejected by requiring  $E/p < 1.0$ . These re-  
 997     quirements combine to remove the majority of isolated electrons and hadrons  
 998     but retain over 95% of the simulated signal across a range of masses and lifetimes.

## 999     11.4 IONIZATION

### 1000    11.4.1 DE/DX CALIBRATION

### 1001    11.4.2 MASS ESTIMATION

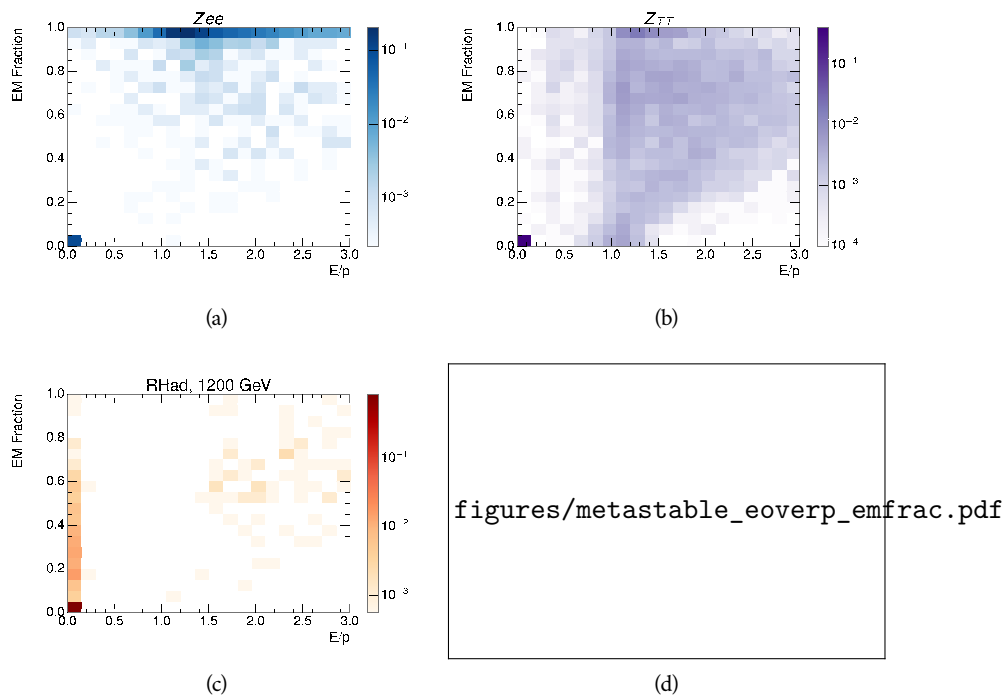


Figure 29: The normalized, two-dimensional distribution of  $E/p$  and  $f_{EM}$  for simulated (a)  $Z \rightarrow ee$ , (b)  $Z \rightarrow \tau\tau$ , (c) 1200 GeV Stable R-Hadron events, and (d) 1200 GeV, 10 ns R-Hadron events.



# 12

1002

1003 BACKGROUND ESTIMATION

---

1004 12.1 BACKGROUND SOURCES

1005 12.2 PREDICTION METHOD

1006 12.3 VALIDATION AND UNCERTAINTY



# 13

1007

1008 SYSTEMATIC UNCERTAINTIES AND RESULTS

---

1009 13.1 SYSTEMATIC UNCERTAINTIES

1010 13.2 FINAL YIELDS



# 14

1011

## 1012 INTERPRETATION

---

### 1013 14.1 CROSS SECTIONAL LIMITS

### 1014 14.2 MASS LIMITS

### 1015 14.3 CONTEXT FOR LONG-LIVED SEARCHES



1016

## PART VI

1017

### CONCLUSIONS

1018

You can put some informational part preamble text here.



# 15

1019

1020 SUMMARY AND OUTLOOK

---

1021 15.1 SUMMARY

1022 15.2 OUTLOOK



1023

## PART VII

1024

## APPENDIX

1025



# A

1026

1027 INELASTIC CROSS SECTION

---



# B

1028

## 1029 APPENDIX TEST

---

1030 Examples: *Italics*, SMALL CAPS, ALL CAPS <sup>1</sup>. Acronym testing: **UML!** (**UML!**) –  
1031 **UML! – UML! (UML!) – UML!s**

This appendix is temporary and is here to be used to check the style of the document.

## 1032 B.1 APPENDIX SECTION TEST

1033 Random text that should take up a few lines. The purpose is to see how sections  
1034 and subsections flow with some actual context. Without some body copy be-  
1035 tween each heading it can be difficult to tell if the weight of the fonts, styles,  
1036 and sizes use work well together.

### 1037 B.1.1 APPENDIX SUBECTION TEST

1038 Random text that should take up a few lines. The purpose is to see how sections  
1039 and subsections flow with some actual context. Without some body copy be-  
1040 tween each heading it can be difficult to tell if the weight of the fonts, styles,  
1041 and sizes use work well together.

## 1042 B.2 A TABLE AND LISTING

1043 Curabitur tellus magna, porttitor a, commodo a, commodo in, tortor. Donec in-  
1044 terdum. Praesent scelerisque. Maecenas posuere sodales odio. Vivamus metus la-  
1045 cus, varius quis, imperdiet quis, rhoncus a, turpis. Etiam ligula arcu, elementum a,  
1046 venenatis quis, sollicitudin sed, metus. Donec nunc pede, tincidunt in, venenatis  
1047 vitae, faucibus vel, nibh. Pellentesque wisi. Nullam malesuada. Morbi ut tellus ut  
1048 pede tincidunt porta. Lorem ipsum dolor sit amet, consectetur adipiscing elit.  
1049 Etiam congue neque id dolor.

1050 There is also a Python listing below Listing 1.

---

1 Footnote example.

LABITUR BONORUM PRI NO	QUE VISTA	HUMAN
fastidii ea ius	germano	demonstratea
suscipit instructior	titulo	personas
quaestio philosophia	facto	demonstrated

Table 2: Autem usu id.

## 1051 B.3 SOME FORMULAS

Due to the statistical nature of ionisation energy loss, large fluctuations can occur in the amount of energy deposited by a particle traversing an absorber element<sup>2</sup>. Continuous processes such as multiple scattering and energy loss play a relevant role in the longitudinal and lateral development of electromagnetic and hadronic showers, and in the case of sampling calorimeters the measured resolution can be significantly affected by such fluctuations in their active layers. The description of ionisation fluctuations is characterised by the significance parameter  $\kappa$ , which is proportional to the ratio of mean energy loss to the maximum allowed energy transfer in a single collision with an atomic electron:

*You might get unexpected results using math in chapter or section heads.*  
*Consider the pdfspacing option.*

$$\kappa = \frac{\xi}{E_{\max}} \quad (2)$$

$E_{\max}$  is the maximum transferable energy in a single collision with an atomic electron.

$$E_{\max} = \frac{2m_e\beta^2\gamma^2}{1 + 2\gamma m_e/m_x + (m_e/m_x)^2},$$

1052 where  $\gamma = E/m_x$ ,  $E$  is energy and  $m_x$  the mass of the incident particle,  $\beta^2 = 1 - 1/\gamma^2$  and  $m_e$  is the electron mass.  $\xi$  comes from the Rutherford scattering cross section and is defined as:

$$\xi = \frac{2\pi z^2 e^4 N_{Av} Z \rho \delta x}{m_e \beta^2 c^2 A} = 153.4 \frac{z^2}{\beta^2} \frac{Z}{A} \rho \delta x \text{ keV},$$

1055 where

- z charge of the incident particle
- $N_{Av}$  Avogadro's number
- Z atomic number of the material
- A atomic weight of the material
- $\rho$  density
- $\delta x$  thickness of the material
- 1057  $\kappa$  measures the contribution of the collisions with energy transfer close to  
 1058  $E_{\max}$ . For a given absorber,  $\kappa$  tends towards large values if  $\delta x$  is large and/or if  
 1059  $\beta$  is small. Likewise,  $\kappa$  tends towards zero if  $\delta x$  is small and/or if  $\beta$  approaches  
 1060 1.

2 Examples taken from Walter Schmidt's great gallery:  
<http://home.vrweb.de/~was/mathfonts.html>

Listing 1: A floating example (listings manual)

---

```
1 for i in xrange(10):
    print i, i*i, i*i*i
print "done"
```

---

1061     The value of  $\kappa$  distinguishes two regimes which occur in the description of  
1062     ionisation fluctuations:

- 1063     1. A large number of collisions involving the loss of all or most of the incident  
1064        particle energy during the traversal of an absorber.

1065        As the total energy transfer is composed of a multitude of small energy  
1066        losses, we can apply the central limit theorem and describe the fluctua-  
1067        tions by a Gaussian distribution. This case is applicable to non-relativistic  
1068        particles and is described by the inequality  $\kappa > 10$  (i. e., when the mean  
1069        energy loss in the absorber is greater than the maximum energy transfer  
1070        in a single collision).

- 1071     2. Particles traversing thin counters and incident electrons under any condi-  
1072        tions.

1073        The relevant inequalities and distributions are  $0.01 < \kappa < 10$ , Vavilov  
1074        distribution, and  $\kappa < 0.01$ , Landau distribution.



- 1076 [1] ATLAS Collaboration. “The ATLAS Simulation Infrastructure”. In: *Eur.*  
1077 *Phys. J. C* 70 (2010), p. 823. doi: [10.1140/epjc/s10052-010-1429-9](https://doi.org/10.1140/epjc/s10052-010-1429-9).  
1078 arXiv: [1005.4568 \[hep-ex\]](https://arxiv.org/abs/1005.4568). SOFT-2010-01.
- 1079 [2] ATLAS Collaboration. “A study of the material in the ATLAS inner de-  
1080 tector using secondary hadronic interactions”. In: *JINST* 7 (2012), P01013.  
1081 doi: [10.1088/1748-0221/7/01/P01013](https://doi.org/10.1088/1748-0221/7/01/P01013). arXiv: [1110.6191 \[hep-ex\]](https://arxiv.org/abs/1110.6191).  
1082 PERF-2011-08.
- 1083 [3] ATLAS Collaboration. *Summary of ATLAS Pythia 8 tunes*. ATL-PHYS-PUB-  
1084 2012-003. 2012. url: <http://cds.cern.ch/record/1474107>.
- 1085 [4] ATLAS Collaboration. “Jet energy measurement with the ATLAS detector  
1086 in proton–proton collisions at  $\sqrt{s} = 7$  TeV”. In: *Eur. Phys. J. C* 73 (2013),  
1087 p. 2304. doi: [10.1140/epjc/s10052-013-2304-2](https://doi.org/10.1140/epjc/s10052-013-2304-2). arXiv: [1112.6426 \[hep-ex\]](https://arxiv.org/abs/1112.6426). PERF-2011-03.
- 1089 [5] ATLAS Collaboration. “Single hadron response measurement and calorime-  
1090 ter jet energy scale uncertainty with the ATLAS detector at the LHC”. In:  
1091 *Eur. Phys. J. C* 73 (2013), p. 2305. doi: [10.1140/epjc/s10052-013-2305-1](https://doi.org/10.1140/epjc/s10052-013-2305-1). arXiv: [1203.1302 \[hep-ex\]](https://arxiv.org/abs/1203.1302). PERF-2011-05.
- 1093 [6] ATLAS Collaboration. “Electron and photon energy calibration with the  
1094 ATLAS detector using LHC Run 1 data”. In: *Eur. Phys. J. C* 74 (2014), p. 3071.  
1095 doi: [10.1140/epjc/s10052-014-3071-4](https://doi.org/10.1140/epjc/s10052-014-3071-4). arXiv: [1407.5063 \[hep-ex\]](https://arxiv.org/abs/1407.5063). PERF-2013-05.
- 1097 [7] ATLAS Collaboration. “Jet energy measurement and its systematic uncer-  
1098 tainty in proton–proton collisions at  $\sqrt{s} = 7$  TeV with the ATLAS detec-  
1099 tor”. In: *Eur. Phys. J. C* 75 (2015), p. 17. doi: [10.1140/epjc/s10052-014-3190-y](https://doi.org/10.1140/epjc/s10052-014-3190-y). arXiv: [1406.0076 \[hep-ex\]](https://arxiv.org/abs/1406.0076). PERF-2012-01.
- 1101 [8] ATLAS Collaboration. “A measurement of the calorimeter response to sin-  
1102 ggle hadrons and determination of the jet energy scale uncertainty using  
1103 LHC Run-1  $pp$ -collision data with the ATLAS detector”. In: (2016). arXiv:  
1104 [1607.08842 \[hep-ex\]](https://arxiv.org/abs/1607.08842). PERF-2015-05.
- 1105 [9] ATLAS Collaboration. “Topological cell clustering in the ATLAS calorime-  
1106 ters and its performance in LHC Run 1”. In: (2016). arXiv: [1603.02934](https://arxiv.org/abs/1603.02934)  
1107 [hep-ex].
- 1108 [10] E. Abat et al. “Study of energy response and resolution of the ATLAS barrel  
1109 calorimeter to hadrons of energies from 20 to 350 GeV”. In: *Nucl. Instrum.*  
1110 *Meth. A* 621.1-3 (2010), pp. 134 – 150. doi: <http://dx.doi.org/10.1016/j.nima.2010.04.054>.

- 1112 [11] P. Adragna et al. "Measurement of Pion and Proton Response and Lon-  
 1113 gitudinal Shower Profiles up to 20 Nuclear Interaction Lengths with the  
 1114 ATLAS Tile Calorimeter". In: *Nucl. Instrum. Meth. A* 615 (2010), pp. 158–  
 1115 181. doi: [10.1016/j.nima.2010.01.037](https://doi.org/10.1016/j.nima.2010.01.037).
- 1116 [12] S. Agostinelli et al. "GEANT4: A simulation toolkit". In: *Nucl. Instrum. Meth.*  
 1117 A 506 (2003), pp. 250–303. doi: [10.1016/S0168-9002\(03\)01368-8](https://doi.org/10.1016/S0168-9002(03)01368-8).
- 1118 [13] N. S. Amelin et al. "Transverse flow and collectivity in ultrarelativistic  
 1119 heavy-ion collisions". In: *Phys. Rev. Lett.* 67 (1991), p. 1523. doi: [10.1103/PhysRevLett.67.1523](https://doi.org/10.1103/PhysRevLett.67.1523).
- 1120 [14] N. S. Amelin et al. "Collectivity in ultrarelativistic heavy ion collisions". In:  
 1121 *Nucl. Phys. A* 544 (1992), p. 463. doi: [10.1016/0375-9474\(92\)90598-E](https://doi.org/10.1016/0375-9474(92)90598-E).
- 1122 [15] B. Andersson, A. Tai, and B.-H. Sa. "Final state interactions in the (nuclear)  
 1123 FRITIOF string interaction scenario". In: *Z. Phys. C* 70 (1996), pp. 499–  
 1124 506. doi: [10.1007/s002880050127](https://doi.org/10.1007/s002880050127).
- 1125 [16] B. Andersson et al. "A model for low-pT hadronic reactions with general-  
 1126 lizations to hadron-nucleus and nucleus-nucleus collisions". In: *Nucl. Phys.*  
 1127 B 281 (1987), p. 289. doi: [10.1016/0550-3213\(87\)90257-4](https://doi.org/10.1016/0550-3213(87)90257-4).
- 1128 [17] H. W. Bertini and P. Guthrie. "News item results from medium-energy  
 1129 intranuclear-cascade calculation". In: *Nucl. Instr. and Meth. A* 169 (1971),  
 1130 p. 670. doi: [10.1016/0375-9474\(71\)90710-X](https://doi.org/10.1016/0375-9474(71)90710-X).
- 1131 [18] L. V. Bravin et al. "Scaling violation of transverse flow in heavy ion col-  
 1132 lisions at AGS energies". In: *Phys. Lett. B* 344 (1995), p. 49. doi: [10.1016/0370-2693\(94\)01560-Y](https://doi.org/10.1016/0370-2693(94)01560-Y).
- 1133 [19] L. V. Bravina et al. "Fluid dynamics and Quark Gluon string model - What  
 1134 we can expect for Au+Au collisions at 11.6 AGeV/c". In: *Nucl. Phys. A* 566  
 1135 (1994), p. 461. doi: [10.1016/0375-9474\(94\)90669-6](https://doi.org/10.1016/0375-9474(94)90669-6).
- 1136 [20] CMS Collaboration. "The CMS barrel calorimeter response to particle  
 1137 beams from 2 to 350 GeV/c". In: *Eur. Phys. J. C* 60.3 (2009). doi: [10.1140/epjc/s10052-009-0959-5](https://doi.org/10.1140/epjc/s10052-009-0959-5).
- 1138 [21] H. S. Fesefeldt. *GHEISHA program*. Pitha-85-02, Aachen. 1985.
- 1139 [22] G. Folger and J.P. Wellisch. "String parton models in Geant4". In: (2003).  
 1140 arXiv: [nucl-th/0306007](https://arxiv.org/abs/nucl-th/0306007).
- 1141 [23] B. Ganhuyag and V. Uzhinsky. "Modified FRITIOF code: Negative charged  
 1142 particle production in high energy nucleus nucleus interactions". In: *Czech.  
 1143 J. Phys.* 47 (1997), pp. 913–918. doi: [10.1023/A:1021296114786](https://doi.org/10.1023/A:1021296114786).
- 1144 [24] M. P. Guthrie, R. G. Alsmiller, and H. W. Bertini. "Calculation of the cap-  
 1145 ture of negative pions in light elements and comparison with experiments  
 1146 pertaining to cancer radiotherapy". In: *Nucl. Instrum. Meth.* 66 (1968), pp. 29–  
 1147 36. doi: [10.1016/0029-554X\(68\)90054-2](https://doi.org/10.1016/0029-554X(68)90054-2).
- 1148 [25] J. Beringer et al. (Particle Data Group). "Review of Particle Physics". In:  
 1149 *Chin. Phys. C* 38 (2014), p. 090001. URL: <http://pdg.lbl.gov>.
- 1150
- 1151
- 1152
- 1153

- 1154 [26] V.A. Karmanov. "Light Front Wave Function of Relativistic Composite  
 1155 System in Explicitly Solvable Model". In: *Nucl. Phys. B* 166 (1980), p. 378.  
 1156 doi: [10.1016/0550-3213\(80\)90204-7](https://doi.org/10.1016/0550-3213(80)90204-7).
- 1157 [27] Hung-Liang Lai, Marco Guzzi, Joey Huston, Zhao Li, Pavel M. Nadolsky,  
 1158 et al. "New parton distributions for collider physics". In: *Phys. Rev. D* 82  
 1159 (2010), p. 074024. doi: [10.1103/PhysRevD.82.074024](https://doi.org/10.1103/PhysRevD.82.074024). arXiv: [1007.2241 \[hep-ph\]](https://arxiv.org/abs/1007.2241).
- 1160 [28] A.D. Martin, W.J. Stirling, R.S. Thorne, and G. Watt. "Parton distributions  
 1161 for the LHC". In: *Eur. Phys. J. C* 63 (2009). Figures from the [MSTW Website](#),  
 1162 pp. 189–285. doi: [10.1140/epjc/s10052-009-1072-5](https://doi.org/10.1140/epjc/s10052-009-1072-5). arXiv: [0901.0002](https://arxiv.org/abs/0901.0002).
- 1163 [29] B. Nilsson-Almqvist and E. Stenlund. "Interactions Between Hadrons and  
 1164 Nuclei: The Lund Monte Carlo, Fritiof Version 1.6". In: *Comput. Phys. Com-  
 1165 mun.* 43 (1987), p. 387. doi: [10.1016/0010-4655\(87\)90056-7](https://doi.org/10.1016/0010-4655(87)90056-7).
- 1166 [30] A. Ribon et al. *Status of Geant4 hadronic physics for the simulation of LHC  
 1167 experiments at the start of LHC physics program*. CERN-LCGAPP-2010-02.  
 1168 2010. URL: <http://lcgapp.cern.ch/project/docs/noteStatusHadronic2010.pdf>.
- 1169 [31] A. Sherstnev and R.S. Thorne. "Parton Distributions for LO Generators".  
 1170 In: *Eur. Phys. J. C* 55 (2008), pp. 553–575. doi: [10.1140/epjc/s10052-008-0610-x](https://doi.org/10.1140/epjc/s10052-008-0610-x). arXiv: [0711.2473](https://arxiv.org/abs/0711.2473).
- 1171 [32] T. Sjöstrand, S. Mrenna, and P. Skands. "A Brief Introduction to PYTHIA  
 1172 8.1". In: *Comput. Phys. Commun.* 178 (2008), pp. 852–867. doi: [10.1016/j.cpc.2008.01.036](https://doi.org/10.1016/j.cpc.2008.01.036). arXiv: [0710.3820](https://arxiv.org/abs/0710.3820).
- 1173 [33] Peter Speckmayer. "Energy Measurement of Hadrons with the CERN AT-  
 1174 LAS Calorimeter". Presented on 18 Jun 2008. PhD thesis. Vienna: Vienna,  
 1175 Tech. U., 2008. URL: <http://cds.cern.ch/record/1112036>.
- 1176
- 1177
- 1178
- 1179
- 1180



1181 DECLARATION

---

1182 Put your declaration here.

1183 *Berkeley, CA, September 2016*

1184

---

Bradley Axen



1185

1186 COLOPHON

1187

Not sure that this is necessary.